European Rotorcraft Forum

MODELING AND CONTROL OF LIFT OFFSET COAXIAL AND TILTROTOR ROTORCRAFT

Tom Berger, Ondrej Juhasz, Mark J. S. Lopez, and Mark B. Tischler
Aviation Development Directorate-Ames, U.S. Army AMRDEC (USA)

Joseph F. Horn,
Department of Aerospace Engineering, The Pennsylvania State University (USA)

Abstract
The US Department of Defense has established an initiative to develop a family of next-generation vertical lift aircraft that will fly farther, faster, and more efficiently than the current fleet of rotorcraft. To accomplish these goals, advanced rotorcraft configurations beyond the single main rotor/tail rotor design must be considered. Two advanced configurations currently being flight tested are a lift offset coaxial rotorcraft with a pusher propeller and a tiltrotor. The US Army Aviation Development Directorate has developed generic high-fidelity flight-dynamics models of these two configurations to provide the government with independent control-system design, handling-qualities analysis, and simulation research capabilities for these types of aircraft. This paper describes the modeling approach used and provides model trim data, linearized stability and control derivatives, and eigenvalues as a function of airspeed. In addition, control allocation for both configurations is discussed.

NOMENCLATURE

$\Delta\theta'_{1c}$	Differential phased lateral cyclic [deg]
$\Delta\theta'_{1s}$	Differential phased longitudinal cyclic [deg]
$\Delta\theta_0$	Differential collective [deg]
δ_a	Aileron deflection [deg]
δ_e	Elevator deflection [deg]
δ_{nac}	Nacelle angle [deg]
δ_r	Rudder deflection [deg]
Δ_{SP}	Swashplate control phasing angle [deg]
ρ	Air density [slugs/ft^3]
θ	Pitch attitude [deg]
θ'_{1c}	Symmetric (or single rotor) phased lateral cyclic [deg]
θ'_{1s}	Symmetric (or single rotor) phased longitudinal cyclic [deg]
θ_0	Symmetric collective [deg]
$\theta_{0_{PP}}$	Pusher propeller collective [deg]
$\theta_{1c_{PP}}$	Pusher propeller monocyclic [deg]
φ	Frequency response phase angle [deg]
L_p	Example of dimensional stability derivative, $L_p \equiv \partial L/\partial p$
L_{δ_a}	Example of dimensional control derivative, $L_{\delta_a} \equiv \partial L/\partial \delta_a$
P	Power [hp]
V	Total true airspeed [kts]

1. INTRODUCTION

In 2009, the US Department of Defense (DoD) established the Future Vertical Lift (FVL) initiative to develop a family of next-generation vertical lift aircraft that will fly farther, faster, and more efficiently than the current fleet of rotorcraft. In order to meet these requirements, advanced rotorcraft configurations beyond the single main rotor/tail rotor design must be considered. Recognizing the challenges inherent in these advanced configurations, the DoD established the Joint Multi-Role (JMR) Technology Demonstrator (TD) program to mitigate the risk associated with the development of FVL[1,2]. Two JMR-TDs are being built and flight tested by Bell (V-280 tiltrotor) and Sikorsky/Boeing (SB>1 lift-offset coaxial helicopter with pusher propeller).

In a parallel effort to the JMR-TD development, the US Army has developed its own high-fidelity flight-dynamics models of generic versions of a lift offset coaxial helicopter with pusher propeller (herein refered to as coaxial-pusher) and tiltrotor aircraft using the comprehensive rotorcraft simulation code HeliUM[3,4]. The models were developed

by the Aviation Development Directorate (ADD) to provide the government with independent control-system design, handling-qualities analysis, and simulation research capabilities for these types of aircraft. The models are generic, and not meant to represent specific aircraft (such as the SB>1 or V-280). However, the same modeling techniques that were used to generate the generic tiltrotor and coaxial-pusher models have been used to model many different rotorcraft configurations in the past, and benefit from extensive validation against flight data and other high-fidelity models of multiple coaxial-pusher and tiltrotor aircraft (e.g., Refs. 3, 5).

The generic tiltrotor and coaxial-pusher models were developed to help answer several key research questions. Among these are:

1. Control allocation: What is the best/optimal way to distribute the moments commanded by the pilot or a control system to each of these aircraft's multiple control effectors that?
2. Response types: What response types/hold modes do pilots prefer at high speed and transition for these configurations?
3. Agility/maneuverability: Does the high-speed capability of these aircraft sacrifice any low-speed agility/maneuverability?

This paper will address the first question, while subsequent papers will address the remaining questions.

To use the models for control system design and piloted simulations, linear models and trim data were extracted from HeliUM at different airspeeds, altitudes, and nacelle angles (in the case of the tiltrotor). The linear models were used to develop a control system gain schedule that is outside of the scope of this paper. A full flight-envelope simulation model that is capable of faster-than-real-time simulation was developed from the linear models and trim data. This model is based on a stitched model architecture[6,7], which falls into the class of quasi-Linear-Parameter-Varying models[8].

This paper provides an overview of the generic coaxial-pusher and tiltrotor flight dynamics models. First, detailed descriptions of the physical aircraft parameters used in HeliUM are provided. Next, variations in trim controls and attitudes with airspeed are provided. This is followed by a discussion of the linear models extracted from HeliUM, including description of key stability and control derivatives, the rotor modes retained in the linear models, and the eigenvalues of the linear models. Subsequently, the model stitching architecture used to simulate the models in real-time is discussed. The control allocation method used to distribute the desired moments to the multiple control effectors is shown for each aircraft. Finally, primary on-axis frequency responses are provided for each aircraft at a range of airspeeds, followed by conclusions.

2. FLIGHT DYNAMICS MODELING

2.1. Overview

The flight dynamics models for both configurations were developed using HeliUM[3,4]. HeliUM uses a finite-element approach to model flexible rotor blades with coupled nonlinear flap/lag/torsion dynamics to capture structural, inertial, and aerodynamic loads along each blade segment. Blade, wing, and fuselage aerodynamics come from nonlinear lookup tables, and the rotor airwakes are modeled using a dynamic inflow model[9]. A multi-body like modeling approach is used to build the aircraft configuration from its independent components (e.g., fuselage, wing, nacelle, etc.)[3], which allows modeling of arbitrary aircraft configurations with multiple rotors. Extensive validation of HeliUM (including with flight data) covering many rotorcraft configurations has previously been done.

HeliUM coaxial-pusher modeling has been validated using Sikorsky X2™ Technology Demonstrator flight data and the Sikorsky X2 GenHel model[5]. HeliUM tiltrotor modeling has been validated against XV-15 flight data, the Bell GTRSIM XV-15 model, and a CAMRAD II[10] (comprehensive analysis tool) model of the Large Civil Tiltrotor (LCTR)[3]. The excellent results of all these validation efforts give confidence in the modeling fidelity and approach used here for the generic aircraft models.

To be able to realistically simulate these aircraft, power required was included in the models. Power requirements in HeliUM are obtained from summing power requirements of the individual main rotors and any tail rotors, with an additional 5% added to account for transmission and accessory losses.

2.2. Coaxial-Pusher

2.2.1. Description

The coaxial-pusher configuration was derived from a previous rotorcraft sizing trade-off study[11], which gives the overall dimensional and weight characteristics as well as key rotor and aircraft aerodynamic properties. The only configuration change made to the original design[11], was to relocate the pusher propeller to be vertically aligned with the aircraft center-of-gravity (CG). This change was made to be more consistent with the X2 and SB>1 configurations, and is the same configuration used in Hersey

et al.[12] The coaxial-pusher aircraft is shown in Figure 1.

Figure 1: Generic coaxial-pusher rendering.

Public domain data of the Sikorsky XH-59A Advancing Blade Concept (ABC)[13] and Sikorsky X2™ Technology Demonstrator were used to develop the mass and stiffness properties for the generic coaxial-pusher hingeless rotor system. Physical blade properties for the XH-59A were tuned such that the first non-dimensional flap and lag mode frequencies are similar to that of the X2, a state-of-the-art aircraft that represents the latest technology advancements in rotor design. Blade twist and chord properties come from the rotor aerodynamic optimization results in Ref. 11. The same blade airfoils were used as the XH-59A ABC.

The inflow model for this configuration immerses each rotor in the wake of the other rotor (using a simple "dynamic climb" approximation) in hover and slow-speed flight using scale factors as defined in Ref. 14. The blending of the inflow diminishes as speed increases, and the two rotors are treated independently at airspeed above $V = 120$ kts. A new technique to extract a higher-fidelity model of inflow from a free wake for the coaxial rotors has been developed by Hersey et al.[12] that provides a lower-order state-space approximation for use in the flight dynamics model. The calculation has been completed for the same generic coaxial-pusher model used herein and shows some important differences for flight control design. Hersey and his coauthors[12] are currently working on validating this higher-fidelity inflow model using flight test data.

Aerodynamics for the H-tail come from open-source lookup tables of XV-15 vertical and horizontal stabilizers obtained from wind tunnel tests that include effects of elevator and rudder deflections[15].

Finally, the pusher propeller is treated as a momentum theory Bailey rotor[16]. It generates a thrust and torque which are transmitted to the aircraft CG. This type of modeling for the pusher propeller has been validated with X2 and SB>1 models and provides a high level of fidelity.

A set of key aircraft properties is given in Table 1. The aircraft gross weight is $35,200$ lbs. Maximum speed is limited to $V = 240$ kts using notional engines that provide a total of $8,000$ hp. The rotors are four-bladed with a radius of $R = 30.55$ ft each. The vertical separation between the rotors is 7% of the rotor diameter, or 4.28 ft. The blades of both rotors are preconed by $\beta_p = 2.0$ deg at the hub to reduce steady flapwise bending stresses.

Table 1: Coaxial-Pusher Configuration Data

Aircraft Data	
Gross Weight	$35,200$ lbs
Max Continuous Power (SL)	$8,000$ hp
V_{MCP} (KTAS, 6k95)	240 kts
Rotor Data	
Radius	30.55 feet
Number of Blades/Rotor	4
Rotational Speed	$23.7 - 19.0$ rad/sec
Vertical Separation (S/D)	7%
Precone	2 deg
Twist	-9 deg
Pusher Data	
Radius	6.6 feet
Number of Blades	6
Rotational Speed	136 rad/sec

2.2.2. Trim

To have a MATLAB Simulink simulation model that is capable of faster-than-real-time execution speeds, linear models and trim data were extracted from HeliUM and used to develop a stitched model of the coaxial-pusher configuration. The stitched model will be described in more detail in Sec. 4, but the coaxial-pusher trim data and linear models are presented here.

To trim the nonlinear HeliUM model, a set of ganged phased controls was used for the coaxial rotors. First, the swashplate cyclic controls (lateral cyclic pitch θ_{1c} and longitudinal cyclic pitch θ_{1s}) for each rotor must be phased since the phase lag between cyclic pitch and flap is significantly less than 90 deg for these very stiff rotors. Figure 2 shows the control phasing notation, where θ'_{1c} and θ'_{1s} are the phased lateral and longitudinal cyclic pitch inputs, and Δ_{SP} is the phase (or mixing) angle. For a fully articulated blade, $\Delta_{SP} = 0$ deg and the primed notation is dropped. Typical values of phase angle are $\Delta_{SP} = 8 - 12$ deg[17]. The optimal phase angle de-

pends on airspeed. For the very stiff coaxial-pusher rotors, a single value of $\Delta_{SP} = 70$ deg, was chosen as a compromise between hover and forward flight. This value of phase angle is similar to the values used for the XH-59A ($\Delta_{SP} = 50 - 60$ deg)[13].

The phased controls for the two rotors were then ganged into symmetric (θ_0, θ'_{1c}, and θ'_{1s}) and differential ($\Delta\theta_0$, $\Delta\theta'_{1c}$, and $\Delta\theta'_{1s}$) rotor controls, with the symmetric controls used to trim the HeliUM model.

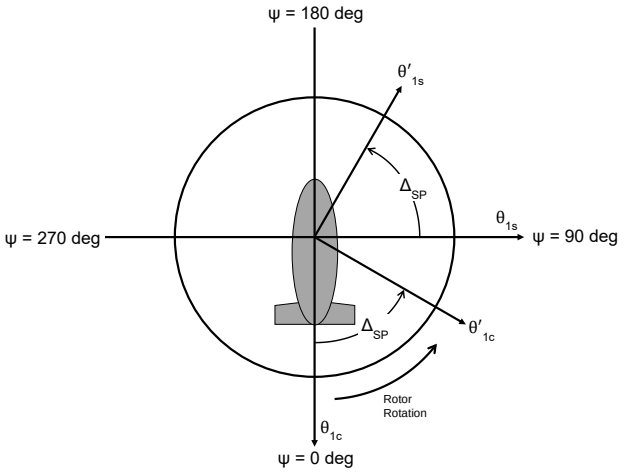

Figure 2: Rotor control phasing definition (coaxial-pusher upper rotor shown).

Note that the control scheme described here is used only to trim the nonlinear model in order to extract linearized models. Once the linearized models were generated, a pseudo inverse control allocation scheme was developed for use in a control system, which led to different (optimal) phasing of the controls, as described in Sec. 3.

The aircraft is trimmed using both the symmetric rotor controls described above and the pusher propeller collective ($\theta_{0_{PP}}$). The pusher propeller provides a redundant control degree of freedom in the longitudinal axis, which allows specific trim attitude targets to be reached. The nominal trim condition is ship level (i.e., $\theta = 0$ deg) at all airspeeds.

Aerosurface controls (elevator δ_e and rudder δ_r) as well as pusher propeller monocyclic $\theta_{1c_{PP}}$ are used for control but not to trim the aircraft.

Figure 3 shows trim values as a function of airspeed for standard sea level conditions. Rotor speed is reduced linearly from NR = 100% ($\Omega = 23.7$ rad/sec) to NR = 80% ($\Omega = 19.0$ rad/sec) between $V = 160 - 220$ kts, and remains at NR = 80% above $V = 220$ kts, to avoid Mach effects on each rotor's advancing blade. A 20% reduction in rotor speed was similarly done for the Sikorsky X2 technology demonstrator aircraft[18].

Trim symmetric collective θ_0 has its maximum value at hover and decreases as airspeed increases.

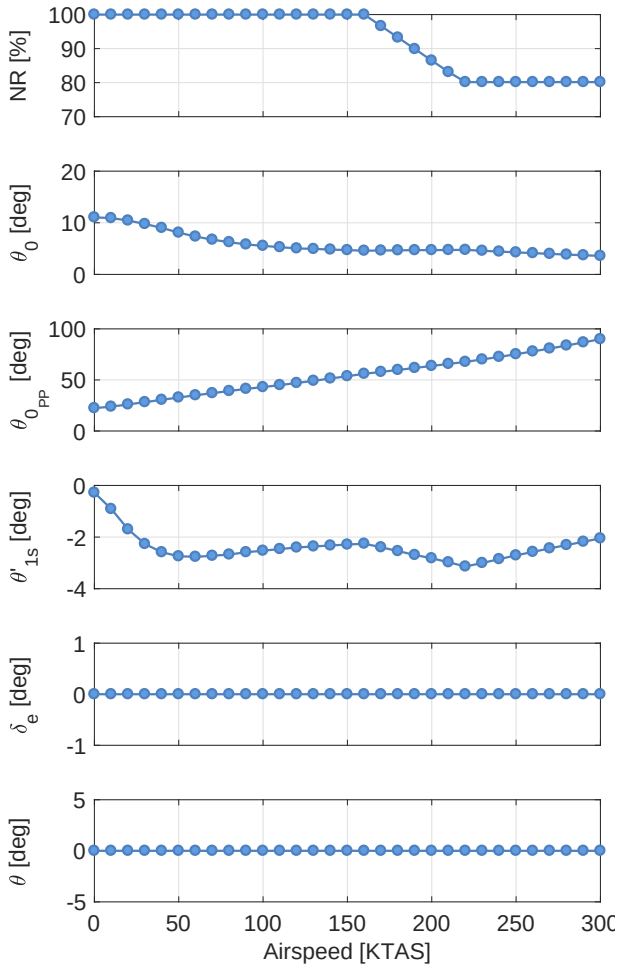

Figure 3: Trim rotor speed (NR), symmetric collective pitch (θ_0), pusher propeller collective pitch ($\theta_{0_{PP}}$), symmetric longitudinal cyclic pitch (θ'_{1s}), elevator (δ_e), and pitch attitude (θ) as a function of airspeed (coaxial-pusher).

This is typical of conventional helicopters[19], where trim collective approaches its minimum value at the minimum drag airspeed and then begins to increase again with increasing airspeed as the rotor is required to provide more propulsive power. However, for the coaxial-pusher configuration, trim symmetric collective continues to decrease with airspeed (increasing slightly between $V = 160 - 220$ kts as rotor speed is decreased), since propulsive power is provided by the pusher propeller.

Trim pusher propeller collective $\theta_{0_{PP}}$ increases linearly from its zero-thrust setting of $\theta_{0_{PP}} = 22.4$ deg up to $\theta_{0_{PP}} = 90.0$ deg at $V = 300$ kts.

Finally, by constraint, elevator δ_e and pitch attitude θ are fixed at $\delta_e = 0$ and $\theta = 0$ for all airspeeds, and pitching moment is trimmed using symmetric longitudinal cyclic θ'_{1s}.

Figure 4 shows the trim power required for the coaxial-pusher as a function of airspeed at standard sea level (SL) conditions and at an altitude of $h = 6,000$ ft and ambient temperature of $T = 95$ F (6k95). The figure also shows the power available P_{avail} provided by a pair of notional engines at sea level and 6k95. Power available for the notional engines is scaled with altitude based on air desity ρ[19]:

$$P_{avail} = P_{avail_{SL}} \frac{\rho}{\rho_{SL}} \quad (1)$$

The notional engines were sized to provide sufficient power to hover at 6k95 and reach speeds of roughly $V = 240$ kts, resulting in $P_{avail_{SL}} = 4,000$ hp per engine.

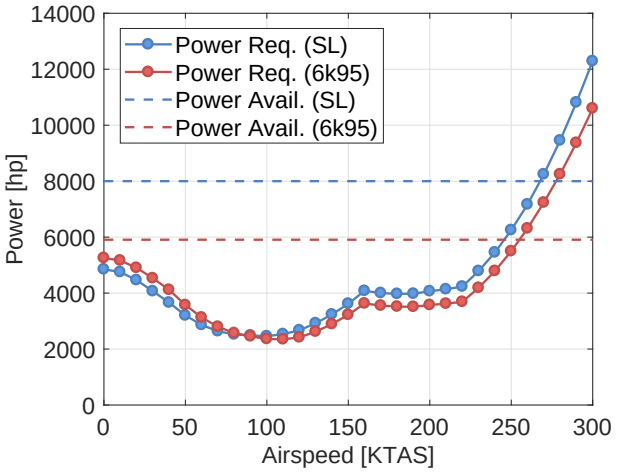

Figure 4: Power required and available at sea level (SL) and 6,000 ft 95 F (6k95) (coaxial-pusher).

2.2.3. Linear Models

Once the HeliUM model was trimmed at specific airspeeds, it was linearized using a numerical linearization algorithm. Linear models were extracted at airspeeds ranging from hover to 300 kts in increments of 10 kts, and at altitudes from sea level to 25,000 ft in increments of 5,000 ft. For brevity, data at sea level only is presented in this paper.

The linear models contain 48 states:

- Nine rigid body states (9),
- Four (one collective, two cyclic, and one reactionless) second-order rotor states for each of the two blade modes retained in the linear model per rotor (32),
- Three (average, cosine, and sine) inflow states per rotor (6),
- One inflow state for the pusher propeller (1).

And 10 inputs:

- Symmetric lateral cyclic (θ'_{1c})
- Symmetric longitudinal cyclic (θ'_{1s})
- Symmetric collective (θ_0)
- Differential collective ($\Delta\theta_0$)
- Differential lateral cyclic ($\Delta\theta'_{1c}$)
- Differential longitudinal cyclic ($\Delta\theta'_{1s}$)
- Pusher propeller collective ($\theta_{0_{PP}}$)
- Pusher propeller monocyclic ($\theta_{1c_{PP}}$)
- Elevator (δ_e)
- Rudder (δ_r)

In addition to all of the states being outputs, power required and tip clearance (discussed later in Sec. 2.2.4) outputs was also included.

The remainder of this section will discuss trends in the linear models as a function of airspeed by looking at the stability and control derivatives, blade modes, and eigenvalues.

To see trends in the rigid body stability and control derivatives of the linear models, the model order was reduced to the six rigid-body degrees-of-freedom (6 DOF), by eliminating all higher-order (rotor and inflow) states enforcing matching DC gains. Figure 5 shows the key rigid-body stability derivatives of the coaxial-pusher as a function of airspeed. Figures 6 and 7 show the key lateral/directional and longitudinal/heave rigid-body control derivatives, respectively, as a function of airspeed.

Stability Derivatives

Speed stability derivative M_u (Figure 5, first row, first column) starts at a positive value ($M_u = 0.036$ rad/sec/ft) in hover. This is due to rotor blowback for increased forward speed. However, this affect is diminished as airspeed increases, and the value of M_u approaches zero above $V = 120$ kts, which is typical of fixed-wing aircraft.

Dihedral effect derivative L_v (Figure 5, second row, first column) is similar to the M_u derivative, although negative in sign due to the body axis system sign convention. It begins at a large value ($L_v = -0.12$ rad/sec/ft) in hover, and decreases in magnitude as airspeed increases. The negative value of L_v, as well as the positive value of N_v (not shown), has a stabilizing effect on lateral/directional static stability[17].

Longitudinal static stability derivative M_w (Figure 5, first row, second column) starts at $M_w \approx 0$ for hover, and becomes larger (more positive) as airspeed increases. Since $M_w > 0$, this aircraft is statically unstable, and the instability becomes more pronounced as airspeed increases, as will be seen in the eigenvalue plots shown later.

Damping derivative L_p**,** M_q (Figure 5, second row, second column, and second row, third column, respectively) are both negative and increase in magnitude with increasing airspeed. Between $V = 160 - 220$ kts, both derivatives decrease linearly as rotor speed is decreased.

Roll coupling derivative L_q (Figure 5, first row, third column) Roll moment due to pitch, given by the L_q derivative is large around hover and decreases with increasing airspeed. Above $V = 100$ kts, the coupling is significantly reduced and L_q is small, common for helicopters in forward flight (e.g., SH-2G identification results in Ref. 7) .

Lateral/Directional Control Derivatives The primary roll control derivative is rolling moment due to symmetric lateral cyclic $L_{\theta'_{1c}}$ (Figure 6, first row, first column). The derivative value starts at $L_{\theta'_{1c}} = 2.12$ rad/sec^2/deg at hover, decreases slightly to a value of $L_{\theta'_{1c}} = 1.92$ rad/sec^2/deg at $V = 40$ kts, and then increases monotonically with increasing airspeed until $V = 160$ kts. Between $V = 160 - 220$ kts as the rotor speed is decreased, $L_{\theta'_{1c}}$ decreases also, but continues to increase above $V = 220$ kts.

Large rolling moments are also generated by differential collective at higher airspeeds as seen by the $L_{\Delta\theta_0}$ derivative (Figure 6, second row, first column). However, this is an undesirable coupling effect as differential collective is intended for yaw control.

The yawing moment generated by differential collective is also a function of airspeed as seen by the $N_{\Delta\theta_0}$ derivative (Figure 6, first row, third column), with its largest value in hover. The $N_{\Delta\theta_0}$ derivative approaches a value of zero for airspeeds greater than $V = 100$ kts. This is because the amount of yawing moment generated through differential collective is proportional to the rotor torque, which for the coaxial-pusher is highest at hover and decreases as airspeed increases (proportional to the trim symmetric collective θ_0 curve in Figure 3).

Side force and yawing moment due to rudder both increase proportional to dynamic pressure or V^2 with increasing airspeed as seen from the Y_{δ_r} (not shown) and N_{δ_r} (Figure 6, second row, last column) derivatives. The rudder is only effective at generating yawing moments at high airspeeds. This leaves a gap in the mid-airspeed range where yawing moment due to differential collective is reduced and the rudder is not effective enough.

Differential longitudinal cyclic $\Delta\theta'_{1s}$ also generates a yawing moment by producing differential torque on the two rotors. It is effective at speeds greater than $V = 50$ kts as seen by the $N_{\Delta\theta'_{1s}}$ derivative (Figure 6, second row, third column). However, it also generates an off-axis rolling moment at low ($V < 50$ kts) and high ($V > 150$ kts) airspeeds, as seen by the $L_{\Delta\theta'_{1s}}$ derivative (Figure 6, first row, second column).

To meet yaw control power and roll-sideslip coupling requirements, a fourth yaw control was introduced—pusher propeller monocyclic $\theta_{1c_{PP}}$. The yaw moment generated by the pusher propeller monocyclic is proportional to the thrust being generated by the pusher propeller and therefore increases with increasing airspeed as seen by the $N_{\theta_{1c_{PP}}}$ derivative (Figure 6, first row, last column). There is also near zero rolling moment generated by pusher propeller monocyclic as seen by the $L_{\theta_{1c_{PP}}}$ derivative (Figure 6, second row, second column), since the pusher propeller is vertically aligned with the CG.

Longitudinal/Heave Control Derivatives The primary pitch control derivative is pitching moment due to symmetric longitudinal cyclic $M_{\theta'_{1s}}$ (Figure 7, second row, third column). This derivative value has a similar variation with airspeed as rolling moment due to symmetric lateral cyclic $L_{\theta'_{1c}}$, however $M_{\theta'_{1s}}$ is smaller in magnitude than $L_{\theta'_{1c}}$ at all airspeeds due to the aircraft's larger pitch inertia I_{yy} than roll inertia I_{xx} (about a factor of 8).

Symmetric longitudinal cyclic θ'_{1s} also generates vertical force, as seen by the $Z_{\theta'_{1s}}$ derivative (Figure 7, second row, first column). This derivative is $Z_{\theta'_{1s}} = 0$ in hover and increases in magnitude above $V = 100$ kts. The primary control for vertical force is symmetric collective θ_0 as seen by the Z_{θ_0} derivative (Figure 7, first row, second column). Symmetric collective also generates a pitching moment (M_{θ_0}), with increasing magnitude as airspeed increases.

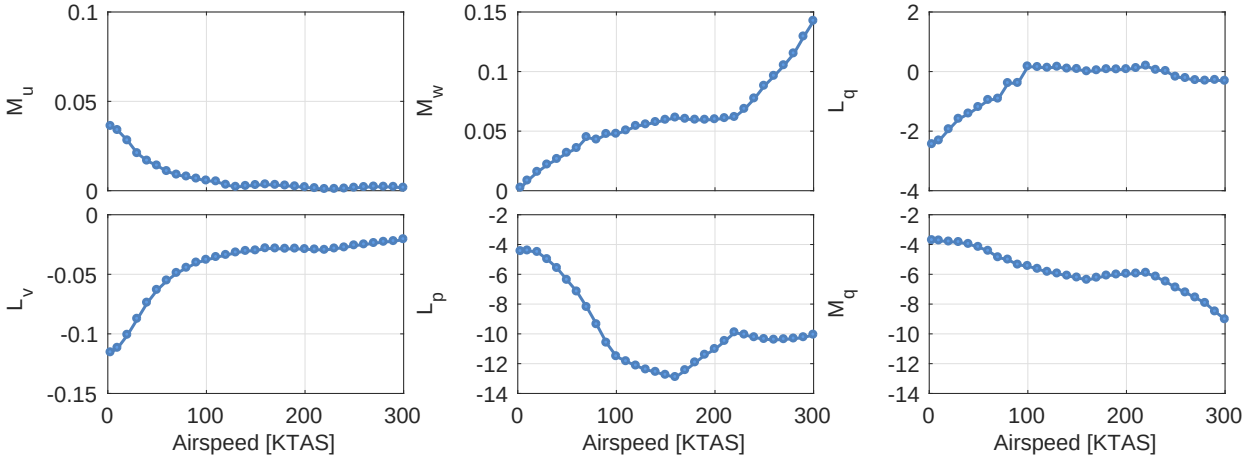

Figure 5: Rigid body stability derivatives as a function of airspeed (coaxial-pusher).

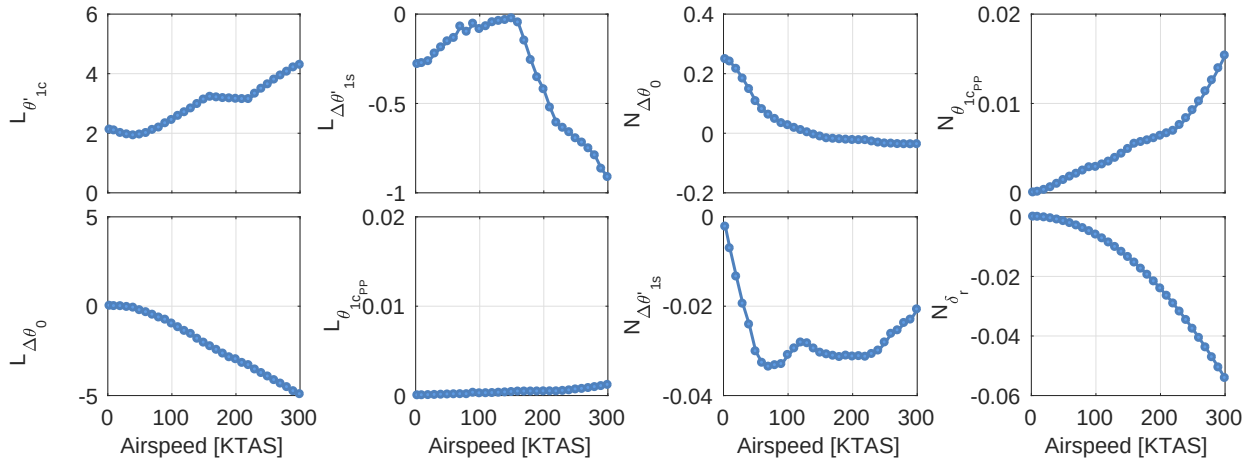

Figure 6: Rigid body lateral/directional control derivatives as a function of airspeed (coaxial-pusher).

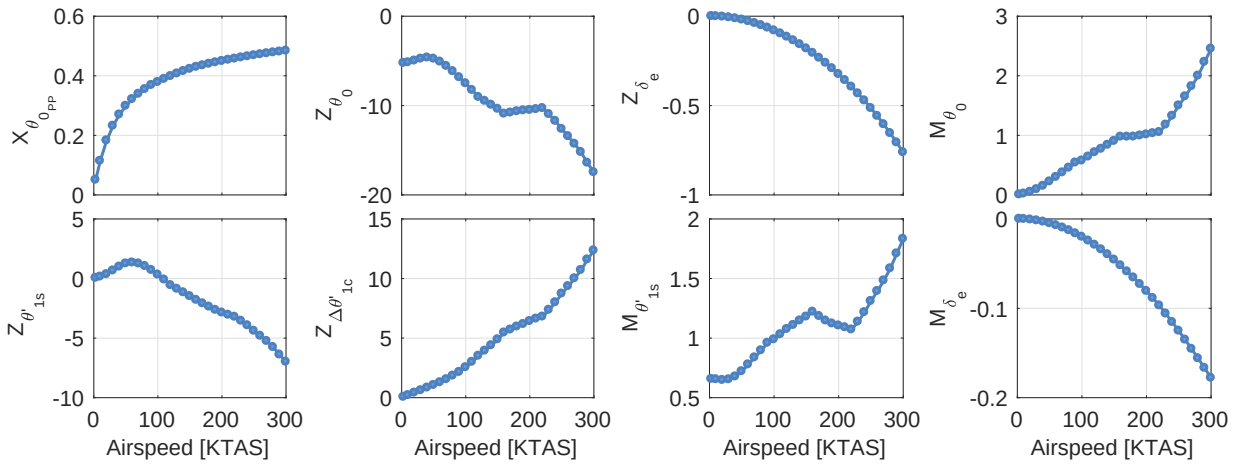

Figure 7: Rigid body longitudinal/heave control derivatives as a function of airspeed (coaxial-pusher).

This can potentially cause undesirable pitch-heave coupling at high speed.

The vertical force generated by differential lateral cyclic $\Delta\theta'_{1c}$ is a strong function of airspeed, as seen by the $Z_{\Delta\theta'_{1c}}$ derivative (Figure 7, second row, second column). Differential lateral cyclic $\Delta\theta'_{1c}$ controls lift offset, and as it is increased, the lift vector on each rotor is moved outboard on the advancing blade and increases in magnitude. Due to the counter rotating rotors, the total rolling moment generated by differential lateral cyclic $L_{\Delta\theta'_{1c}}$ (not shown) is nearly zero.

Axial force is provided by the pusher propeller collective $\theta_{0_{PP}}$ as seen by the $X_{\theta_{0_{PP}}}$ derivative (Figure 7, first row, first column). The amount of force generated per degree of pusher propeller collective is small at low airspeeds and increases with airspeed. Pitching moment due to pusher propeller collective is nearly zero due to the pusher propeller being vertically aligned with the CG. However, rolling moment due to pusher propeller collective is significant due to the increased torque on the propeller with increased thrust.

Normal force and pitching moment due to elevator both increase proportional to dynamic pressure or V^2 with increasing airspeed as seen from the Z_{δ_e} (Figure 7, first row, third column) and M_{δ_e} (Figure 7, second row, last column) derivatives .

Blade Modes The first two rotor blade modes (coupled flap-lag) are retained in the linearized coaxial-pusher models. Figure 8 shows the natural frequencies of the two modes in the rotating frame as a function of rotor speed, with the primary motion (first flap bending 1F or first lag bending 1L) labeled. Note that the mode frequencies shown here are for constant collective θ_0 value. At $\Omega/\Omega_0 = 1$, the lag mode frequency is $\nu_\zeta = 1.33$/rev (stiff in-plane), while the flap mode frequency is $\nu_\beta = 1.49$/rev. For the range of rotor speed used $\Omega/\Omega_0 = 0.8 - 1$, the two blade modes are away from any integer rotor harmonics (e.g., 1/rev, 2/rev, etc.).

Figure 9 shows the flap and lag blade deflections contributing to each of the two blade modes for the nominal rotor speed (Ω) and reduced rotor speed (0.8Ω). At the nominal rotor speed Ω_0, the lower frequency Mode 1 is primarily composed of the first lag mode with some contribution of the first flap mode (Figure 9, upper plot, solid lines). The higher frequency Mode 2 at the nominal rotor speed Ω_0 is primarily composed of first flap mode with some contribution of the first lag mode (Figure 9, lower plot, solid lines).

At the reduced rotor speed $0.8\Omega_0$, the flap and lag modes become nearly fully coupled, with Mode 1 being anti-symmetric flap-lag motion (Figure 9, upper plot, dashed lines) and Mode 2 being symmetric flap-lag motion (Figure 9, lower plot, dashed lines). This coupling of the modes as the rotor is slowed down can be seen from the convergence of the two mode lines in Figure 8 at around $\Omega/\Omega_0 = 0.8$. As the rotor is slowed down further ($\Omega/\Omega_0 < 0.8$), the modes decouple and switch dominant motion. This behavior was similarly seen in the XH-59A[13].

The blade modes are stable for all airspeeds as will be shown in the eigenvalue analysis next.

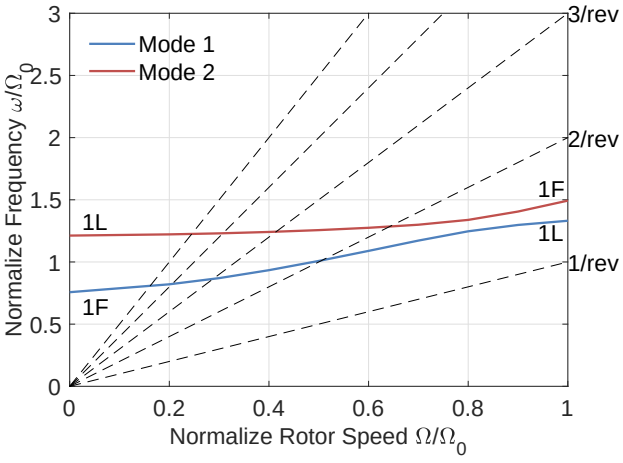

Figure 8: Blade mode fan diagram (coaxial-pusher).

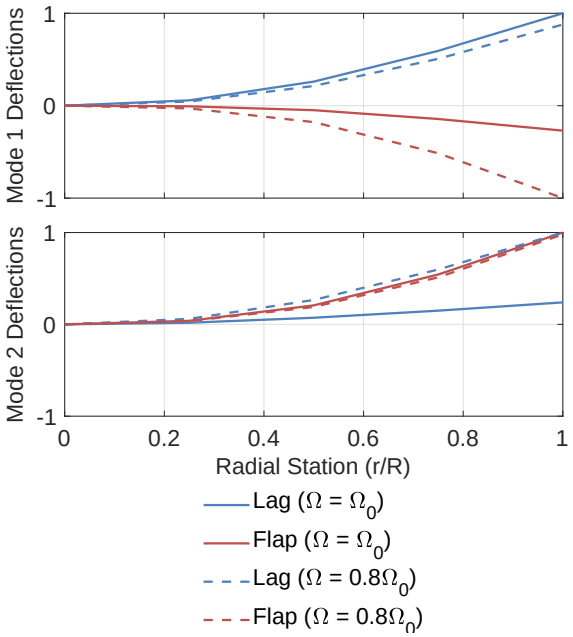

Figure 9: Flap and lag deflections for blade Modes 1 and 2 (coaxial-pusher).

Eigenvalues Figures 10 and 11 show a zoomed-out and zoomed-in view, respectively, of the eigenvalues of the full order (48-state) linear state-space models as a function of airspeed. The collective, progressive, regressive, and reactionless rotor modes can be seen in Figure 10. These rotor modes correspond to blade Mode 1 and Mode 2, and are labeled with their dominant motion (flap and lag) as discussed in the previous section. Note that there are two of each mode (for the two rotor), for a total of 16 modes.

The rotor modes are all stable, with the lag mode being more lightly damped than the flap mode, as expected. Furthermore, the rotor mode frequencies are a function of rotor speed, mainly varying between $V = 160 - 220$ kts where the rotor is slowed down. The two (low-frequency) regressive flap modes couple with the fuselage roll and pitch motion.

In addition, the six inflow modes can be seen in Figure 10, which are a strong functions of airspeed with natural frequencies roughly equal to the rotor speed and damping ratios between $\zeta = 0.76 - 1.0$ throughout.

Figure 11 shows the fuselage eigenvalues of the coaxial-pusher as a function of airspeed. At hover, there are low-frequency unstable complex modes (hovering cubic) in both the lateral (marked Dutch Roll in Figure 11) and longitudinal (marked Phugoid in Figure 11) axes. In the lateral axis, this mode stabilizes and increases in frequency as airspeed increases, becoming the lightly damped Dutch roll mode. In the longitudinal axis, the complex pair of the phugoid mode is also unstable at hover and low speed, but reduces in frequency and becomes stable as airspeed increases.

A real roll mode ($1/T_r$) is present which increases in frequency with increasing airspeed, from about $1/T_r = 5$ rad/sec at hover to $1/T_r = 10$ rad/sec at $V = 300$ kts. These values of roll mode inverse time constant correspond to the values of the L_p derivative seen in Figure 5.

As expected from the positive values of M_w seen in Figure 5, the short period mode of the coaxial-pusher is unstable. The short period remains composed of two real poles—one stable (labeled "Pitch" in Figure 11) and one unstable (labeled "Short Period" in Figure 11) for all airspeeds, with both poles increasing in frequency with increasing airspeed.

Finally, low frequency real yaw and heave modes can be in Figure 11. These modes also increase in frequency with increasing airspeed.

2.2.4. Tip Clearance Output

Ensuring sufficient separation between the two rotors of the coaxial-pusher configuration during dynamic maneuvers is important. Therefore, a tip clearance output was added to the linear models. This was done by first performing a state transformation on the linear models, transforming states corresponding to blade Modes 1 and 2 into states corresponding to flap and lag. Then, the values of the flap states were used to determine the location of the tip path plane of each rotor. Finally, the minimum distance between the two tip path planes around the azimuth was determined.

Figure 12 shows the trim minimum rotor separation as a function of airspeed. Minimum rotor separation is an indirect measure of lift offset. Increasing lift offset increases loading on each rotor's advancing side, causing the tip path planes of the two rotors to get closer on one side and further away on the other. The decreasing trim minimum rotor separation with increasing airspeed is consistent with increasing lift offset on the two rotors.

2.3. Tiltrotor

2.3.1. Description

The generic tiltrotor configuration was derived from scaling geometric, inertial, and structural properties of the XV-15[20,21,22], V-22[23], and the notional NASA Large Civilian Tilt-Rotor 2 (LCTR2)[24,25]. The resulting tiltrotor aircraft is shown in Fig. 13, and is similar to the configuration used in the control allocation study in Ref. 26.

The generic tiltrotor has a stiff in-plane hingeless rotor system with non-dimensional flap and lag modes similar to the LCTR2. The same airfoils were used as in the LCTR2. Baseline blade properties for twist and chord are derived from the XV-15 and tuned to be consistent with trends from more advanced tiltrotors like the V-22 and LCTR2.

The wings are scaled geometrically with data from the other tiltrotors, but do not have any forward wing sweep to remain consistent with V-280 design. The wings have both inboard flaps and outboard ailerons similar to the XV-15. The flaps are schedule with airspeed and nacelle angle to retract in forward flight and extend in hover.

The inflow model for this configuration leaves the wake of each rotor isolated. The wake impinges on the wing and results in an additional down force in hover.

Aerodynamics for the V-tail come from lookup tables of representative airfoils. The V-tail flaperons can deflect symmetrically (equivalent elevator deflection δ_e) to produce a pitching moment or asym-

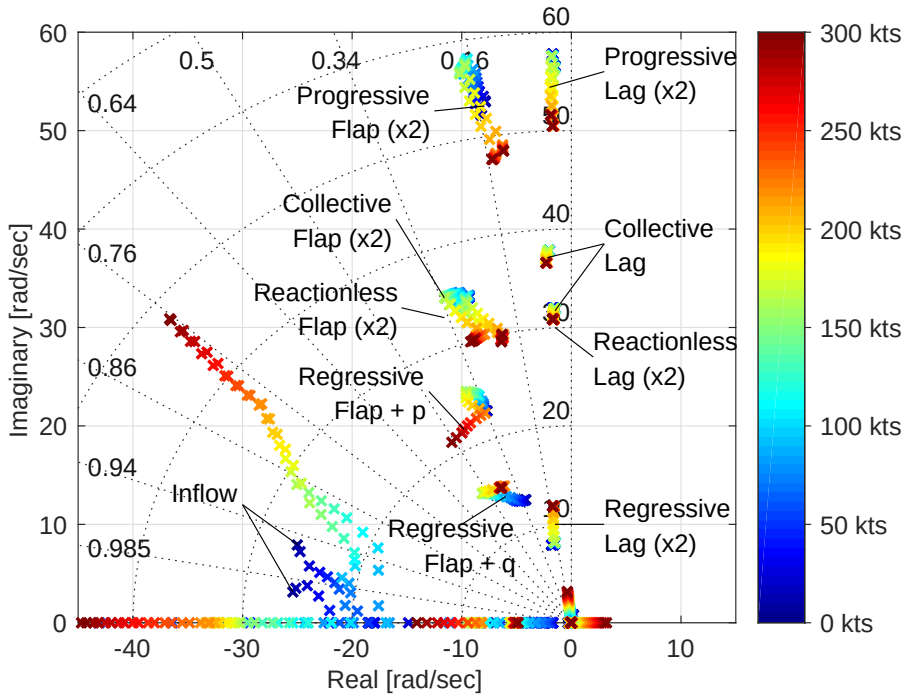

Figure 10: Eigenvalues as a function of airspeed (coaxial-pusher).

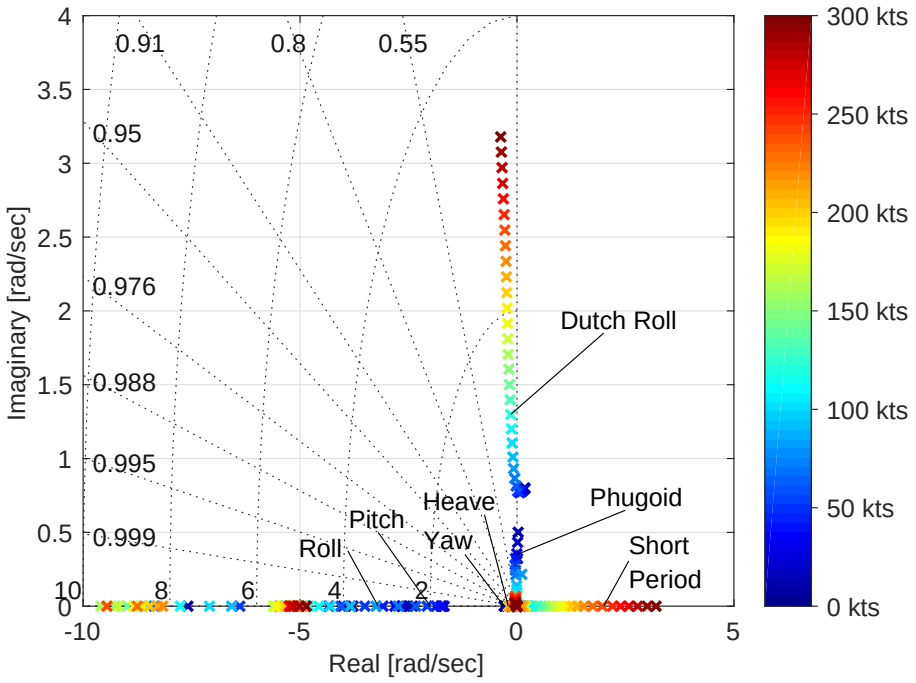

Figure 11: Low-frequency eigenvalues as a function of airspeed (coaxial-pusher).

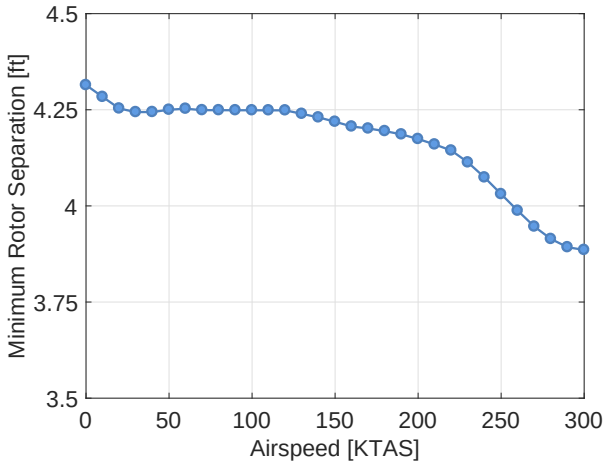

Figure 12: Minimum rotor separation as a function of airspeed (coaxial-pusher).

Table 2: Tiltrotor Configuration Data

Aircraft Data	
Gross Weight	$32,100$ lbs
Max Continuous Power (SL)	$9,400$ hp
V_{MCP} (KTAS, 6k95)	280 kts
Wing Span	45 ft
Wing Sweep	0 deg
Nacelle Range	$0-95$ deg
Rotor Data	
Radius	17.8 feet
Number of Blades/Rotor	4
Rotational Speed	$40-30$ rad/sec
Precone	2.5 deg
Twist	-44 deg

metrically (equivalent rudder deflection δ_r) to produce a yawing moment.

A set of key aircraft properties is given in Table 2. The aircraft gross weight is $32,100$ lbs. Maximum speed is limited to $V = 280$ kts using notional engines that provide a total of $9,400$ hp. The rotors are four-bladed with a radius of $R = 17.8$ ft each. The blades of both rotors are preconed by $\beta_p = 2.5$ deg at the hub to reduce steady flapwise bending stresses. Furthermore, the blades have a significant amount of pretwist $\theta_{tw} = -44$ deg for these proprotors.

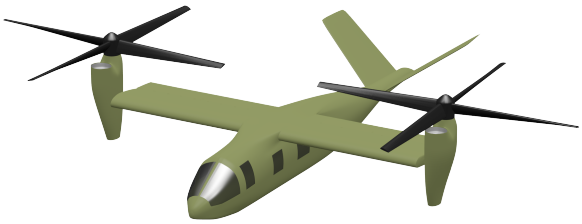

Figure 13: Generic tiltrotor rendering.

2.3.2. Trim

Similarly to the coaxial-pusher HeliUM model, the tiltrotor HeliUM model was used to generate a set of linear models and trim data at the flight conditions spanning the conversion corridor shown in Figure 14. Figure 15 shows the trim control and pitch attitude values for the tiltrotor as a function of airspeed and nacelle angle. As with the coaxial-pusher, the tiltrotor rotor controls are phased and ganged into symmetric (collective θ_0, lateral cyclic θ'_{1c}, and longitudinal cyclic θ'_{1s}) and differential (collective $\Delta\theta_0$, lateral cyclic $\Delta\theta'_{1c}$, and longitudinal cyclic $\Delta\theta'_{1s}$) controls. For the tiltrotor, a phase angle of $\Delta_{SP} = 50$ deg was chosen to minimize the off-axis flapping response.

The rotor speed NR is schedule with nacelle angle (Figure 15, top plot) and is reduced from NR $=$ 100% ($\Omega = 40$ rad/sec) to NR $=$ 75% ($\Omega = 30$ rad/sec) when the nacelles are at $\delta_{nac} = 0$ deg (airplane mode).

Symmetric longitudinal cyclic θ'_{1s} (Figure 15, second plot) is used for trim for nacelle angles $\delta_{nac} > 0$ deg, but phased out in airplane mode ($\delta_{nac} = 0$ deg).

Trim collective θ_0 (Figure 15, third plot) begins at a similar value for all nacelle angles in hover. Below minimum drag speed $V \approx 70$ kts (region where induced drag dominates), less trim collective is required as airspeed is increased. Additionally, for a give airspeed, less trim collective is required for lower nacelle angles. This is because the aircraft is trimmed at a higher pitch attitude θ for lower nacelle angles (Figure 15, last plot), which translates to larger angle-of-attack α on the wing. Therefore, for lower nacelle angles, the lift share of the wing is higher and the rotor has to generate less lift. Above $V \approx 70$ kts (region where profile drag dominates), both trends are reversed. More trim collective is required for higher airspeeds, to overcome the increased drag. In addition, more trim collective is required for lower nacelle angles. This is because at high speed, a lower angle-of-attack α (achieved with higher nacelle angles) results in reduced profile drag.

Finally, unlike the coaxial-pusher, elevator deflec-

tion δ_e is used to trim the tiltrotor (Figure 15, fourth plot).

Figure 16 shows the trim power required for the tiltrotor as a function of airspeed at standard sea level conditions and at an altitude of $h = 6,000$ ft and ambient temperature of $T = 95$ F (6k95). The figure also shows the power available P_{avail} provided by a pair of notional engines at sea level and 6k95. The notional engines were sized to provide sufficient power to hover at 6k95 and reach speeds of roughly $V = 280$ kts, resulting in $P_{avail_{SL}} = 4,700$ hp per engine.

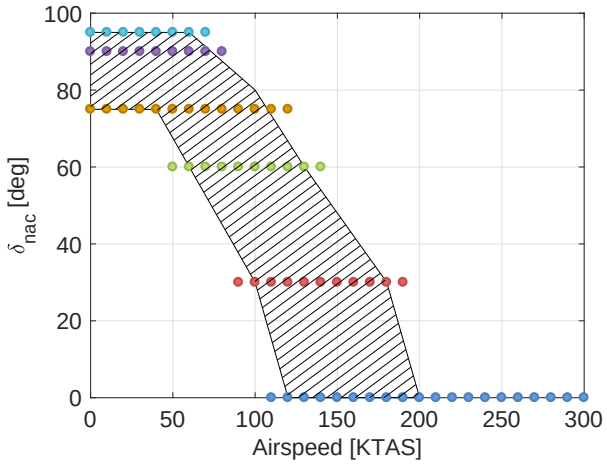

Figure 14: Conversion corridor and linear model points (tiltrotor).

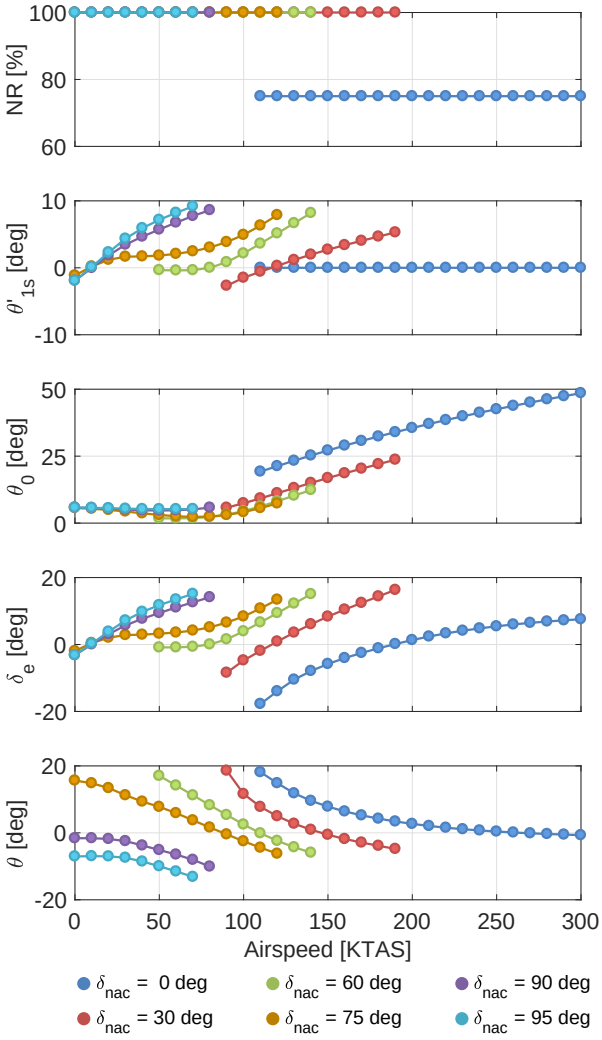

Figure 15: Trim rotor speed (NR), symmetric longitudinal cyclic pitch (θ'_{1s}), symmetric collective pitch (θ_0), elevator (δ_e), and pitch attitude (θ) as a function of airspeed and nacelle angle (tiltrotor).

2.3.3. Linear Models

Once trimmed, the HeliUM tiltrotor model was linearized at specific airspeeds and nacelle angles spanning the conversion corridor, shown as the points in Figure 14. This was repeated for several altitudes from sea level to 25,000 ft in increments of 5,000 ft. For brevity, data at sea level only is presented in this paper.

The tiltrotor linear models contain 51 states:

- Nine rigid body states (9),
- Four (one collective, two cyclic, and one reactionless) second-order rotor states for each of the two blade modes retained in the linear model per rotor (32),
- Three (average, cosine, and sine) inflow states per rotor (6),
- Second order nacelle angle dynamics per nacelle (4).

And 10 inputs:

- Symmetric lateral cyclic (θ'_{1c})

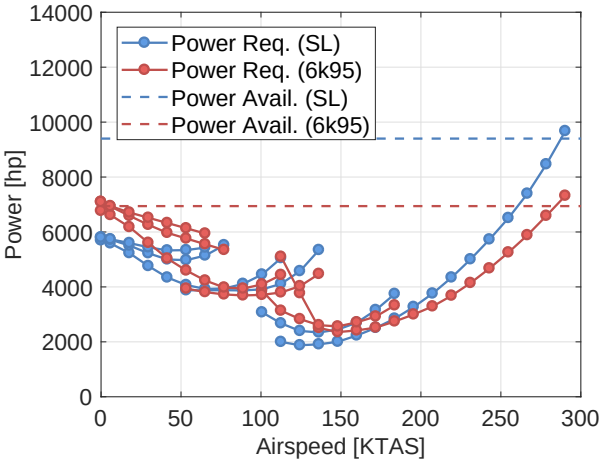

Figure 16: Power required and available at sea level (SL) and 6,000 ft 95 F (6k95) (tiltrotor).

- Differential collective ($\Delta\theta_0$)
- Symmetric longitudinal cyclic (θ'_{1s})
- Symmetric collective (θ_0)
- Differential longitudinal cyclic ($\Delta\theta'_{1s}$)
- Aileron (δ_a)
- Elevator (δ_e)
- Rudder (δ_r)
- Nacelle 1 torque (Q_{nac_1})
- Nacelle 2 torque (Q_{nac_2})

The nacelle torque inputs are the torques required to maintain the nacelles at their current angles by the nacelle actuators. A simple PID control system is used to convert commanded nacelle angles δ_{nac_1} and δ_{nac_2} to the required torques Q_{nac_1} and Q_{nac_2}, modeling the nacelle angle actuators.

Before further analysis was done, the two individual nacelle angle inputs and states were transformed to symmetric (δ_{nac}) and differential ($\Delta\delta_{nac}$) nacelle angles, with only symmetric nacelle angle deflections considered here.

As in the case of the coaxial-pusher model, in addition to all of the states being outputs, a power required output was also included in the linear models.

The remainder of this section will discuss trends in the linear models as a function of airspeed by looking at the stability and control derivatives, blade modes, and eigenvalues.

Stability Derivatives

Speed stability derivative M_u (Figure 17, first row, first column) starts at a positive value in hover for all nacelle angles. As in the case of the coaxial-pusher the value of M_u approaches zero as airspeed increases. At high airspeeds with the nacelles at $\delta_{nac} = 0$ deg, $M_u \approx 0$ which is typical of fixed-wing aircraft.

Longitudinal static stability derivative M_w (Figure 17, second row, first column) starts at $M_w \approx 0$ for hover, and becomes larger in magnitude (more negative) as airspeed increases. Since $M_w < 0$, this aircraft is statically stable in forward flight.

Rate damping derivatives L_p, M_q, N_r (Figure 17, first row, second column; first row, third column; second row, third column) are all negative and increase in magnitude with increasing airspeed. At airspeeds above $V \approx 100$ kts, the roll rate damping derivative L_p value is a function of nacelle angle δ_{nac}, with larger magnitude (more negative) for lower nacelle angle. This is because the contribution of the rotors to L_p decreases as the nacelle angle decreases and the rotors become less aligned with the airflow resulting from the aircraft rolling. This is in contrast to the pitch rate damping derivative M_q values which are similar for different nacelle angle δ_{nac} for $V > 100$ kts, since the main contribution is from the tailplane.

Coupling derivatives L_q, M_q (Figure 17, second row, second column, L_q only shown) are essentially zero for the tiltrotor due to its symmetric configurations, as is the case for the smaller XV-15 tiltrotor aircraft[7].

Lateral/Directional Control Derivatives In hover, rolling moment can be generated using differential collective $\Delta\theta_0$ as well as symmetric lateral cyclic θ'_{1c}, as seen by the values of the $L_{\Delta\theta_0}$ (Figure 18, first row, first column) and $L_{\theta'_{1c}}$ (Figure 18, second row, first column) control derivatives. The values of $L_{\Delta\theta_0}$ increase in magnitude with increasing airspeed, and decrease with decreasing nacelle angle. As the nacelles are rotated down towards airplane mode ($\delta_{nac} = 0$ deg), differential collective $\Delta\theta_0$ generates less rolling moment and more yawing moment, with $N_{\Delta\theta_0}$ (Figure 18, second row, third column) remaining constant with airspeed but increasing in magnitude with decreasing nacelle angle.

Differential longitudinal cyclic $\Delta\theta'_{1s}$ is the primary yaw control in hover/low-speed with $N_{\Delta\theta'_{1s}}$ (Figure 18, first row, last column) having the largest magnitude of the yaw control derivatives for airspeeds below $V \approx 90$ kts.

Rolling moment due to aileron increases proportional to dynamic pressure or V^2 with increasing airspeed as seen from the L_{δ_a} derivative (Figure 18, second row, second column). Similarly, yawing moment due to rudder increases proportional to V^2 as seen by the N_{δ_r} derivative (Figure 18, second row, last column). Unique to the V-tail configuration of the tiltrotor, effective rudder deflection δ_r also generates large rolling moment, with roughly equal magnitudes of L_{δ_r} (Figure 18, first row, third column) and N_{δ_r}. Furthermore, the roll generated due to effective rudder deflection δ_r is adverse ($L_{\delta_r} < 0$, $N_{\delta_r} > 0$), with a left-wing-down roll moment being generated for nose-right yaw moment. This undesired behavior should be addressed with the flight controls through control mixing.

Longitudinal and heave responses due to lateral/directional inputs are essentially zero due to the symmetric rotor configuration.

Longitudinal/Heave Control Derivatives The primary pitch control derivative at hover/low-speed is pitching moment due to symmetric longitudinal cyclic $M_{\theta'_{1s}}$ (Figure 19, second row, third column).

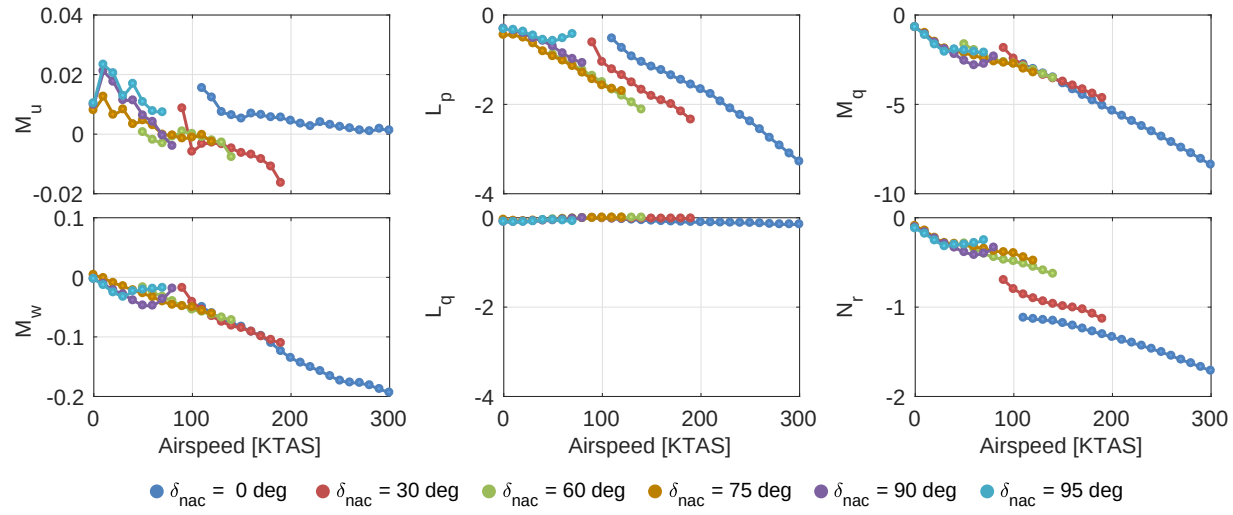

Figure 17: Rigid body stability derivatives as a function of airspeed (tiltrotor).

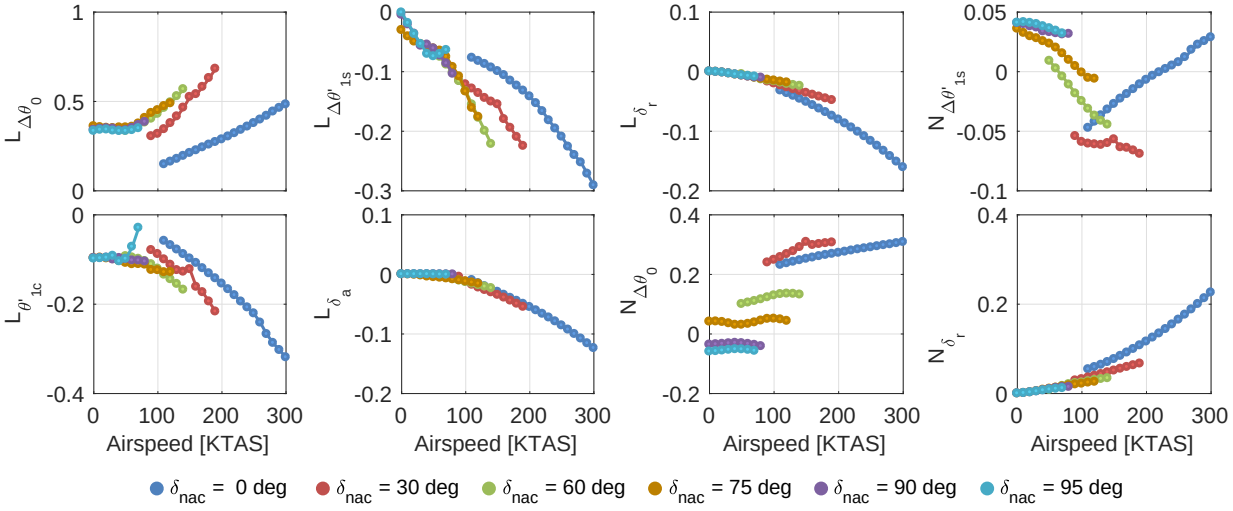

Figure 18: Rigid body lateral/directional control derivatives as a function of airspeed (tiltrotor).

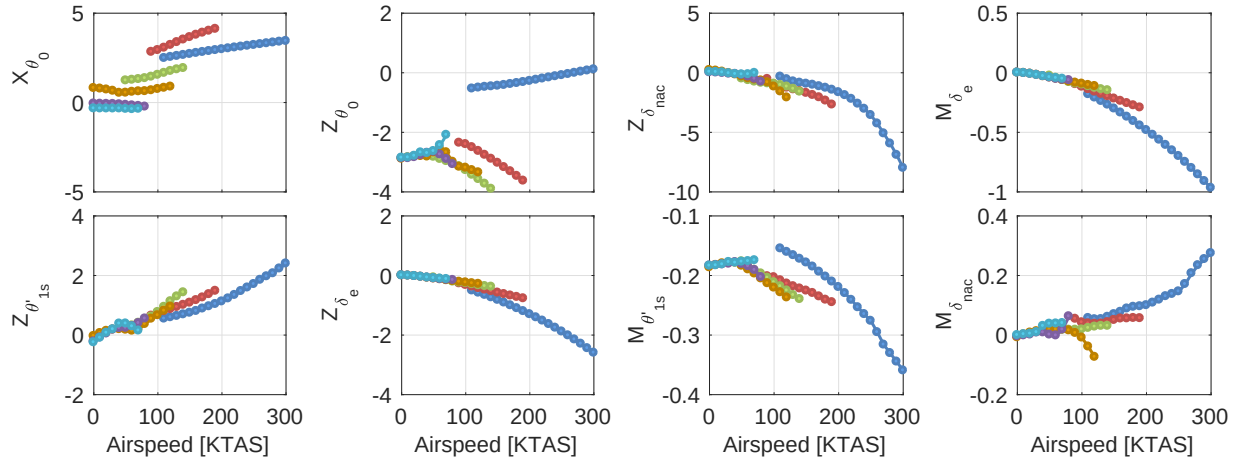

Figure 19: Rigid body longitudinal/heave control derivatives as a function of airspeed (tiltrotor).

This derivative has a similar variation with airspeed and nacelle angle as rolling moment due to symmetric lateral cyclic $L_{\theta'_{1c}}$. Symmetric longitudinal cyclic also generates z-axis force, as seen by the $Z_{\theta'_{1s}}$ derivative (Figure 19, second row, first column), with its value increasing with increasing airspeed.

In hover/low-speed, the primary control for z-axis force is symmetric collective θ_0, as seen by the Z_{θ_0} derivative (Figure 19, first row, second column). As airspeed is increased and nacelle angle is reduced to $\delta_{\text{nac}} = 0$, the primary control for pitching moment and z-axis force is effective elevator δ_{e}, with its effectiveness increasing proportional to dynamic pressure or V^2 with increasing airspeed, as seen by $M_{\delta_{\text{e}}}$ (Figure 19, first row, last column) and $Z_{\delta_{\text{e}}}$ (Figure 19, second row, second column).

Increasing nacelle angle tilts the thrust vector up, creating a negative z-axis force, as seen by the negative values of the $Z_{\delta_{\text{nac}}}$ derivative (Figure 19, first row, third column). The magnitude of $Z_{\delta_{\text{nac}}}$ is proportional to the amount of thrust generated by the rotors, which increases with airspeed. Similarly, the pitching moment generated by the nacelles $M_{\delta_{\text{nac}}}$ (Figure 19, second row, last column) increases with airspeed.

Blade Modes As with the coaxial-pusher linear models, two coupled flap-lag rotor blade modes are retained in the linearized tiltrotor models. Figure 20 shows the natural frequencies of the two modes as a function of rotor speed. The primary motion (flap or lag) of the modes are not labeled because they are nearly fully coupled. Figure 21 shows the flap and lag blade deflections due to each of the two blade modes for the nominal rotor speed ($\Omega = \Omega_0 = 40$ rad/sec) and reduced rotor speed ($\Omega = 0.75\Omega_0 = 30$ rad/sec).

Two main differences between the coaxial-pusher and tiltrotor blade modes are: 1) the flap and lag modes are more tightly coupled for the tiltrotor, and 2) the second tiltrotor blade mode is at a higher normalized frequency ($\nu_{\text{Mode2}} = 2.48$/rev at $\Omega/\Omega_0 = 1$). Both of these differences are due to the large amount of pretwist of the tiltrotor's proprotor blades ($\theta_{\text{tw}} = -44$ deg, Table 2) as compared to the coaxial-pusher rotor blades ($\theta_{\text{tw}} = -9$ deg, Table 1).

Pretwist introduces structural coupling between flap and lag deflections[27], which causes Mode 1 to have nearly equal magnitude deflections in the flap and lag directions for both $\Omega = \Omega_0$ and $\Omega = 0.75\Omega_0$ (Figure 21, upper plot).

Pretwist also pulls the blade loading inboard, leading to aerodynamic distribution with a shape closer to the second flap and lag modes, which results in greater contributions of these higher modes[28]. For the tiltrotor, the lag deflection of Mode 2 (Figure 21, lower plot, blue line) has a shape which includes the second bending mode (with the slope of the deflection changing direction at the outboard portion of the blade). Therefore, blade Mode 2 includes first bending mode in flap coupled with first and second bending modes in lag, and hence has a higher frequency than the coaxial-pusher Mode 2.

At both the nominal ($\Omega/\Omega_0 = 1$) and reduced ($\Omega/\Omega_0 = 0.75$) rotor speeds, Modes 1 and 2 are deconflicted from any of the integer rotor harmonics (e.g., 1/rev, 2/rev, etc.). However, Mode 2 does cross the 3/rev harmonic at around $\Omega/\Omega_0 = 0.8$. Dwelling in this region of rotor speed can be avoided by introducing hysteresis in the rotor speed nacelle angle schedule.

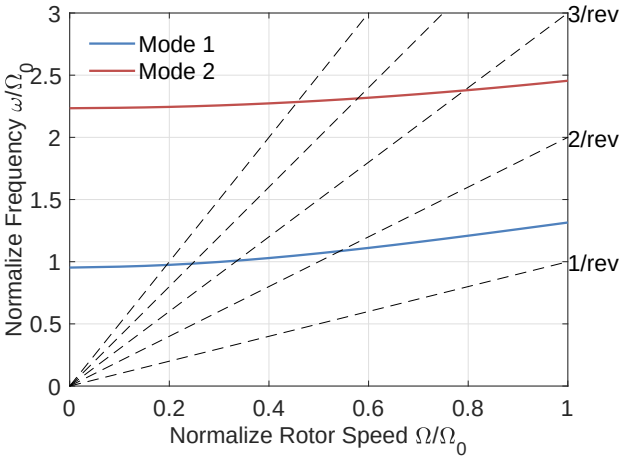

Figure 20: Blade mode fan diagram (tiltrotor).

Eigenvalues Figures 22 and 23 show a zoomed-out and zoomed-in view, respectively, of the eigenvalues of the full-order (51-state) linear state-space models plus nacelle controllers (2-state) as a function of airspeed and nacelle angle. The collective, progressive, regressive, and reactionless rotor modes can be seen in Figure 22. These rotor modes correspond to blade Mode 1 and Mode 2 discussed in the previous section. Unlike the coaxial-pusher eigenvalues (Figure 10), here the rotor modes are not labeled with their dominant motion since the rotor modes are nearly fully coupled. Note that there are two of each mode (for the two rotor), for a total of 16 modes.

The tiltrotor rotor modes appear to be much stronger functions of airspeed than the coaxial-pusher rotor modes (Figure 22), with the tiltrotor modes varying the most in airplane mode ($\delta_{\text{nac}} = 0$ deg). This is because the tiltrotor has a much wider trim collective θ_0 range (Figure 15, third plot)

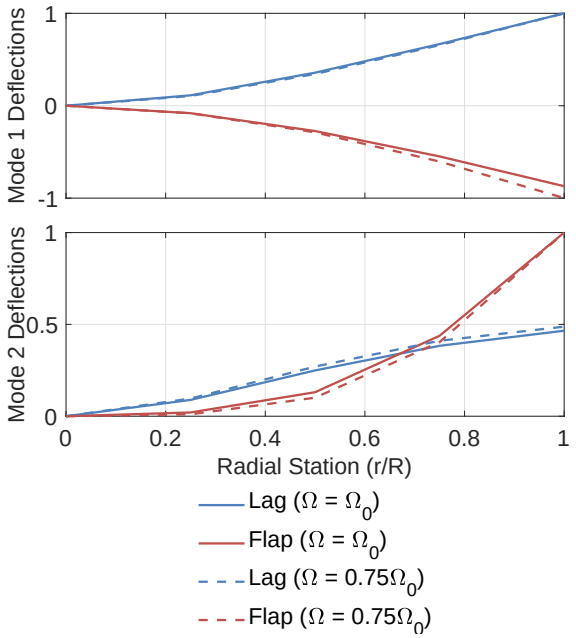

Figure 21: Flap and lag deflections for blade Modes 1 and 2 (tiltrotor).

as compared to the coaxial-pusher (Figure 3, third plot). The rotor modes are all stable, with the lower-frequency Mode 1 being more lightly damped than the higher-frequency Mode 2.

Inflow state modes can be seen in Figure 22 around the rotor speed frequency ($\omega = 30 - 40$ rad/sec). In addition, high-frequency nacelle angle modes can be seen at around $\omega = 60 - 120$. These modes are well damped ($\zeta > 0.9$) due to the inclusion of the nacelle controller described above.

Figure 23 shows the fuselage eigenvalues of the tiltrotor as a function of airspeed and nacelle angle. At hover, there are low-frequency unstable complex modes (hovering cubic) in both the lateral (marked Dutch Roll in Figure 23) and longitudinal (marked Phugoid in Figure 23) axes. In the lateral axis, this mode stabilizes and increases in frequency as airspeed increases, becoming the lightly damped Dutch roll mode ($\zeta_{\text{dr}} = 0.16 - 0.34$). In the longitudinal axis, the oscillatory phugoid mode reduces in frequency and becomes stable as airspeed increases. Eventually, as airspeed continues to increase, the phugoid mode becomes critically damped and turns into two real modes.

As expected from the negative values of M_w seen in Figure 17, the short period mode of the tiltrotor is stable and well damped ($\zeta_{\text{sp}} \approx 0.5$). The short period mode increases in frequency with increasing airspeed.

A real roll mode ($1/T_{\text{r}}$) is present which increases in frequency with increasing airspeed, from about $1/T_{\text{r}} = 0.3$ rad/sec at hover to $1/T_{\text{r}} = 3.5$ rad/sec at $V = 300$ kts. These values of roll mode inverse time constant correspond to the values of the effective L_p derivative seen in Figure 17.

Finally, low frequency real yaw and heave modes can be seen in Figure 23. These modes also increase in frequency with increasing airspeed.

3. CONTROL ALLOCATION

3.1. Overview

A control allocation scheme is required for both the coaxial-pusher and tiltrotor aircraft, since both have redundant controls. A weighted pseudo-inverse method[29,26] is used to allocate the demanded roll, pitch, and yaw moments $\boldsymbol{d}$ to each aircraft's control actuator commands $\boldsymbol{u}_{\text{cmd}}$:

$$\boldsymbol{u}_{\text{cmd}} = \boldsymbol{W}^{-1}\boldsymbol{B}_{\text{RB}}^{T}\left(\boldsymbol{B}_{\text{RB}}\boldsymbol{W}^{-1}\boldsymbol{B}_{\text{RB}}^{T}\right)^{-1}\boldsymbol{d} \tag{2}$$

where $\boldsymbol{W}$ is a diagonal weighting matrix composed of the individual w_i weightings (Eq. 3) and $\boldsymbol{B}_{\text{RB}}$ is the control effectiveness matrix, composed of the $\dot{p}$, $\dot{q}$, and $\dot{r}$ rows of the rigid-body control matrix.

The weightings w_i are based on the actuator rate limits $\dot{\boldsymbol{u}}_{\text{max}}$:

$$w_i = \frac{1}{(\dot{u}_{i_{\text{max}}})^2} \tag{3}$$

The rigid-body control matrix, derived by reducing out the rotor, inflow, and nacelle angle states from the linearized coaxial-pusher and tiltrotor models, is used to get the effective rigid-body control derivatives. In the full-order system, the controls only affect the rotor modes which then affect rigid body motion though the stability matrix $\boldsymbol{A}$. Therefore using the full-order control matrix $\boldsymbol{B}$ would result in incorrect control allocation.

The following sections present the control allocation for both aircraft as a function of airspeed on radar charts, with each spoke corresponding to a bare-airframe input. The control allocation to the individual swashplate actuators was phased and ganged into the symmetric and differential rotor controls presented earlier.

3.2. Coaxial-Pusher Control Allocation

Figure 24 shows the coaxial-pusher roll, pitch, and yaw control allocation as a function of airspeed. Recall from Sec. 2.2.2, the coaxial-pusher controls are phased (denoted by the primed cyclic pitch inputs θ'_{1c} and θ'_{1s}) using a constant phase angle. As shown here, the control allocation introduces some additional phasing that is a function of airspeed.

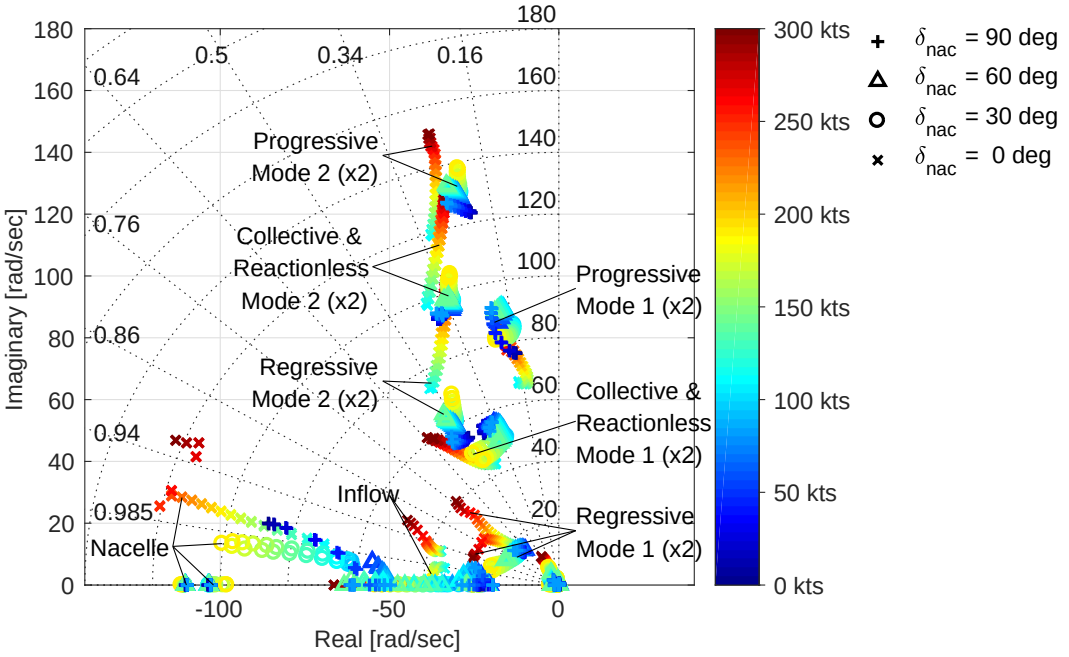

Figure 22: Eigenvalues as a function of airspeed (tiltrotor).

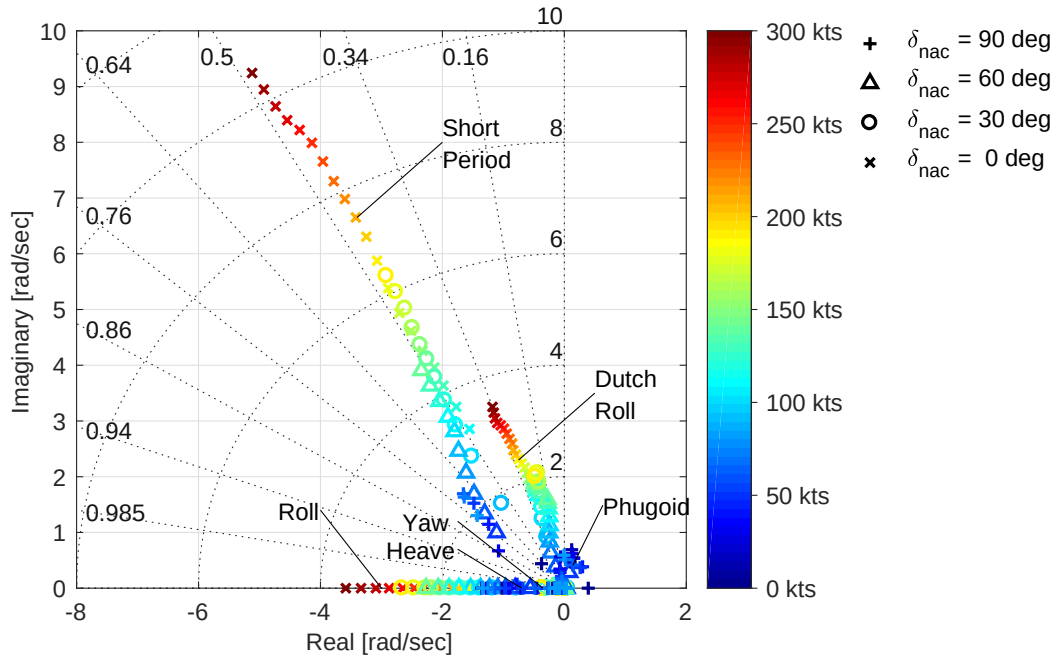

Figure 23: Low-frequency eigenvalues as a function of airspeed (tiltrotor).

In hover, roll moment demand is allocated to symmetric lateral cyclic θ'_{1c}. Some differential longitudinal cyclic $\Delta\theta'_{1s}$ is also used, which phases the symmetric lateral cyclic input. The amount of phasing required increases with airspeed, until it reached a maximum amount at around $V = 100$ kts, as seen by the length of the $\Delta\theta'_{1s}$ spoke. For airspeeds faster than $V = 100$ kts, the amount of phasing required is decreased. As airspeed is increased, differential collective $\Delta\theta_0$ and rudder δ_r are used to remove the bare-airframe yaw-due-to-roll control coupling.

In hover, pitching moment demand is allocated to symmetric longitudinal cyclic θ'_{1s} and symmetric collective θ_0. Note that some differential lateral cyclic $\Delta\theta'_{1c}$ is used, which phases the symmetric longitudinal cyclic input. The amount of phasing required increases with airspeed, as seen by the increases length of the $\Delta\theta'_{1c}$ spoke with increased airspeed. As airspeed increases, less pitching moment demand is allocated to symmetric collective θ_0, with that control being phased out by about $V = 120$ kts. As airspeed continues to increase, more pitching moment demand is allocated to the elevator δ_e.

Yaw moment demand is allocated to differential collective $\Delta\theta_0$ at hover. As airspeed increases, pusher propeller monocyclic $\theta_{1c_{PP}}$, rudder δ_r and differential longitudinal cyclic $\Delta\theta'_{1s}$ are phased in. Differential longitudinal cyclic $\Delta\theta'_{1s}$ is phased out at around $V = 110$ kts, and pusher propeller monocyclic $\theta_{1c_{PP}}$ is phased out at around $V = 150$ kts. At airspeeds faster than $V = 150$ kts, yaw moment is allocated to the rudder only.

3.3. Tiltrotor Control Allocation

Figure 25 shows the tiltrotor control allocation as a function of airspeed and nacelle angle. In hover with the nacelles at $\delta_{nac} = 90$ deg, roll control is achieved using differential collective $\Delta\theta_0$ and symmetric lateral cyclic θ'_{1c}. Differential longitudinal cyclic $\Delta\theta'_{1s}$ is used to remove the yaw-due-to-roll control coupling. As airspeed is increased with the nacelles at $\delta_{nac} = 90$ deg, effective rudder δ_r is also used to remove the yaw-due-to-roll control coupling. This is equivalent to the control crossfeed in the XV-15 (Ref. 7).

With the nacelles at $\delta_{nac} = 60$ deg, roll control is also achieved using differential collective $\Delta\theta_0$ and symmetric lateral cyclic θ'_{1c}, with aileron δ_a fading in with increased airspeed. With the nacelles tilted down ($\delta_{nac} < 90$ deg), differential longitudinal cyclic $\Delta\theta'_{1s}$ is used to generate roll moment as well as yaw moment. Furthermore, effective rudder δ_r deflections are used for roll moment as well (due to the V-tail configuration).

For $\delta_{nac} = 30$ deg, roll control is provided primarily through differential longitudinal cyclic $\Delta\theta'_{1s}$, ailerons δ_a, and rudder δ_r. In airplane mode ($\delta_{nac} = 0$ deg), roll control is provided through ailerons δ_a. Differential longitudinal cyclic $\Delta\theta'_{1s}$ is used to supplement the ailerons in airplane mode to provide sufficient control authority to meet the MIL-STD-1797B[30] time to bank requirement.

Pitch control is achieved though symmetric longitudinal cyclic θ'_{1s}, symmetric collective θ_0, and elevator δ_e. For nacelle angles greater than $\delta_{nac} = 0$ deg, all three controls are used, with the demanded pitch moment allocation to rotor controls (θ'_{1s} and θ_0) decreasing and pitch moment allocation to aerosurface controls (δ_e) increasing with increasing airspeed. For $\delta_{nac} = 0$ deg (airplane mode), demanded pitch moment is allocated to the elevator δ_e only, with decreasing amount as airspeed increases and the elevator becomes more effective.

Finally, with the nacelles at $\delta_{nac} = 90$ deg, yaw control is achieved through differential longitudinal cyclic at hover $\Delta\theta'_{1s}$. As airspeed increases, rudder δ_r is used as well. Differential collective $\Delta\theta_0$ and symmetric lateral cyclic θ'_{1c} are used to remove the roll-due-to-yaw control coupling. With the nacelles at $\delta_{nac} = 60$ deg, as airspeed increases, demanded yaw moment allocation decreases to rotor controls are increases to the aerosurface control. For $\delta_{nac} = 30$ deg, rudder δ_r is the primary yaw control, with some demanded yaw moment being allocated to the rotor. In airplane mode ($\delta_{nac} = 0$ deg), demanded yaw moment is allocated to the rudder δ_r only, with decreasing amount as airspeed increases and the rudder becomes more effective.

4. STITCHED MODEL

4.1. Overview

The linearized models and trim data extracted from HeliUM and presented above were used to developed a stitched simulation model of each aircraft[6,7], which can be run in real-time. At its core, the stitched model is comprised of a quasi-linear-parameter-varying (qLPV) model, with distinctive features specific to aircraft and rotorcraft applications.

A block diagram schematic of the stitched model is shown in Figure 26 (duplicated from Ref. 7). Note that in this schematic the model is only stitched with x-body axis velocity U. To summarize, model stitching is accomplished by implementing lookup tables of the aircraft state trim values, control input trim values, and stability and control derivatives based on linear models and trim data extracted from HeliUM. Trim states and controls are used to deter-

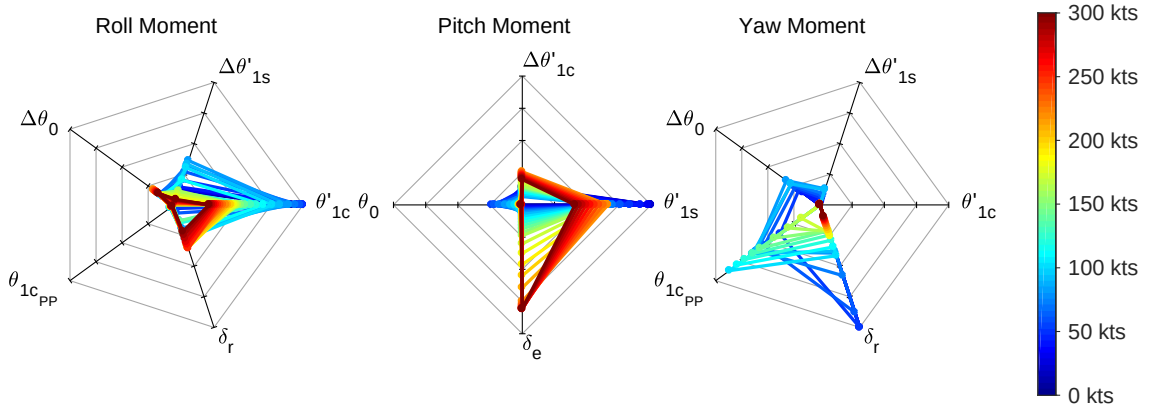

Figure 24: Roll, pitch, and yaw moment control allocation as a function of airspeed (coaxial-pusher).

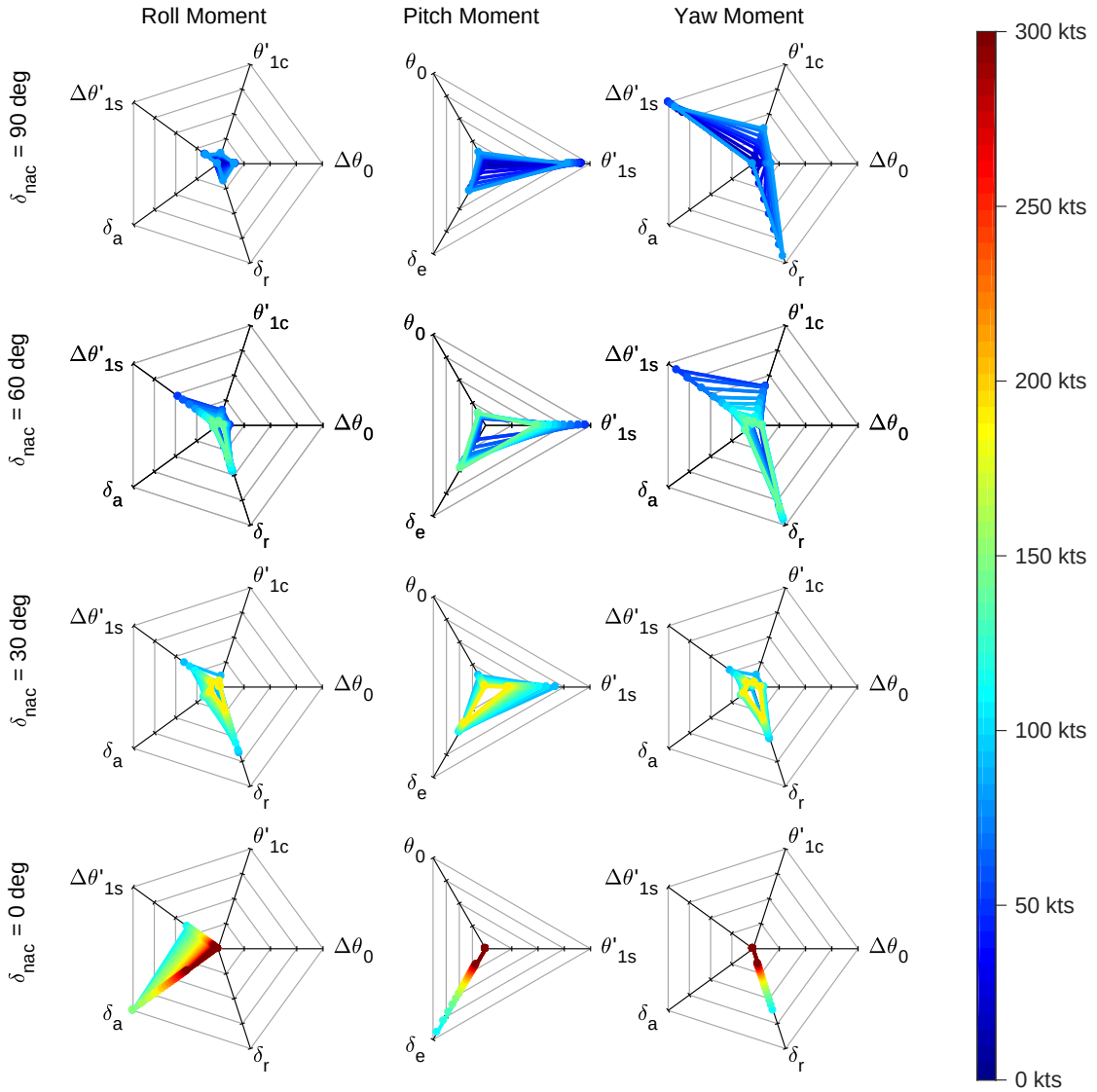

Figure 25: Roll, pitch, and yaw moment control allocation as a function of nacelle angle and airspeed (tiltrotor).

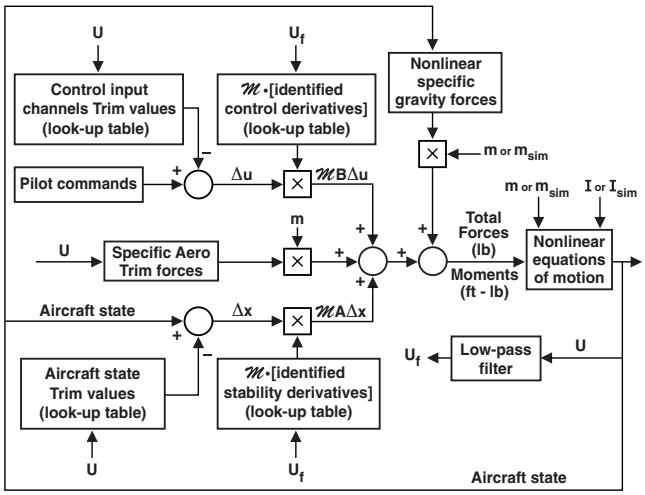

Variable	Description
U	Total longitudinal body axis velocity
U_f	Filtered velocity
$\triangle u$	Control perturbations (e.g., δ_e)
$\triangle x$	State perturbations [e.g., $w \equiv (W - W_0)$]
$\mathcal{M}$	Mass and inertia matrix
A	Dimensional stability derivatives
B	Dimensional control derivatives
m	Aircraft mass
I	Aircraft inertia matrix

Figure 26: Model stitching block diagram schematic[7].

mine perturbation states [$\Delta \boldsymbol{x} = \left(\boldsymbol{X} - \boldsymbol{X}_0(U)\right)$] and controls [$\Delta \boldsymbol{u} = \left(\boldsymbol{U} - \boldsymbol{U}_0(U)\right)$], which in turn are multiplied by the stability and control derivatives and mass matrix ($\boldsymbol{\mathcal{M}A}\Delta \boldsymbol{u}$ and $\boldsymbol{\mathcal{M}B}\Delta \boldsymbol{x}$) to determine perturbation aerodynamic and control forces and moments. Note that the stability and control derivatives are determined based on a low-pass filtered U_f, to ensure that the derivative values remain constant for short-term motion and retain the accurate dynamic response at the discrete point models. Trim values are determined based on instantaneous U, to preserve correct speed derivatives (e.g., X_u, M_u, etc.). The aerodynamic trim forces and moments are then summed to the perturbation values to yield the total aerodynamic forces and moments acting on the aircraft in body axes. The linearized Coriolis terms (e.g., $W_0 q$, etc., due to formulating equations of motion in body axes) and linearized gravity terms normally included in the $\boldsymbol{A}$ and $\boldsymbol{B}$ state-space matrices are removed and added downstream in their nonlinear form.

For the coaxial-pusher, the stitched model is stitched in total longitudinal body axis velocity U and scheduled with altitude. For the tiltrotor the stitched model is stitched in total longitudinal body axis velocity U and symmetric nacelle angle and scheduled with altitude.

The stitched models can be trimmed, simulated, and linearized at any flight condition within the flight envelope of the aircraft. They can also be used to extrapolate the models to different weight, inertia, and CG values. In addition, they contain three-point landing gear models to allow simulation of landing on moving ships. The stitched models have been used for control law development and piloted simulations. The following subsections provide primary on-axis frequency responses of the linearized stitched model at several flight conditions. To generate the frequency responses, the control allocation described in Sec. 3 was included with the stitched model.

4.2. Coaxial-Pusher

Figures 27 through 31 show the primary on-axis frequency responses of the coaxial-pusher stitched model. Figure 27 shows the roll rate p to roll moment demand δ_{lat} frequency responses between hover and 250 kts. In hover, the roll rate response exhibits the unstable lateral phugoid at $\omega = 0.85$ rad/sec. The roll mode real pole (which along with the unstable lateral phugoid makes up the hovering cubic) is at $1/T_r = -L_p = 5$ rad/sec. The regressive flap mode can be seen as the peak at $\omega = 22$ rad/sec (corresponding to the eigenvalue labeled "Regressive Flap + p" in Figure 10), followed by the progressive flap mode at $\omega = 50$ rad/sec.

At $V = 50$ kts, the ω_ϕ complex pair of zeros[31] are present in the roll rate response at around the same frequency as the Dutch roll mode ($\omega_{\text{dr}} = 0.7$ rad/sec), flattening out the low-frequency asymptote. Furthermore, the Dutch roll mode damping is nearly $\zeta_{dr} = 0$ (corresponding to the eigenvalue labeled "Dutch Roll" in Figure 11). The rotor modes are similar to the hover case.

As airspeed increases, several trends can be seen: 1) the Dutch roll mode frequency increases and the ω_ϕ zeros more closely cancel the Dutch roll contribution to the roll response, 2) the roll mode increases in frequency to about $1/T_r = -L_p = 10$ rad/sec at $V = 250$ kts, 3) the regressive flap mode increases in frequency to about $\omega = 28$ rad/sec at $V = 250$ kts, and 4) the progressive flap mode decreases in frequency to about $\omega = 48$ rad/sec at $V = 250$ kts. This is consistent with the variation of the rotor modes with airspeed seen in Figure 10.

Figure 28 shows the pitch rate q to pitch moment

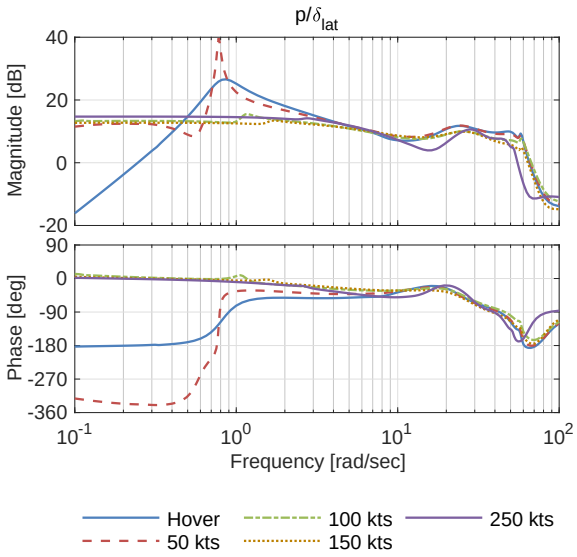

Figure 27: Roll rate frequency response (coaxial-pusher).

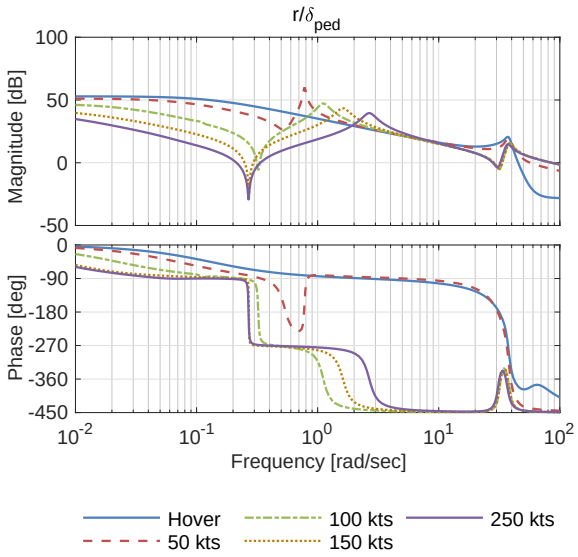

Figure 29: Yaw rate frequency response (coaxial-pusher).

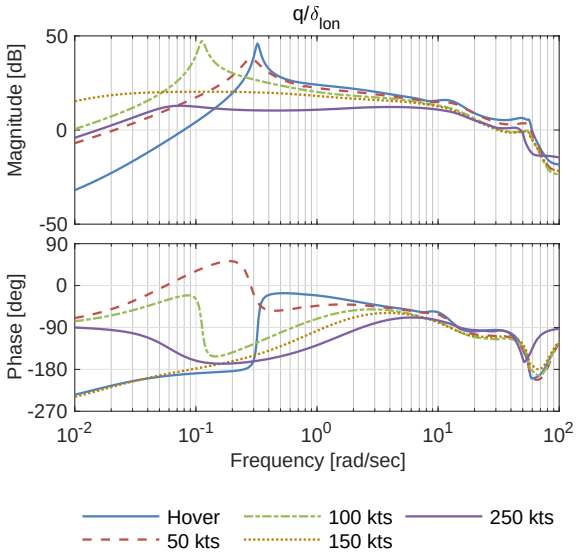

Figure 28: Pitch rate frequency response (coaxial-pusher).

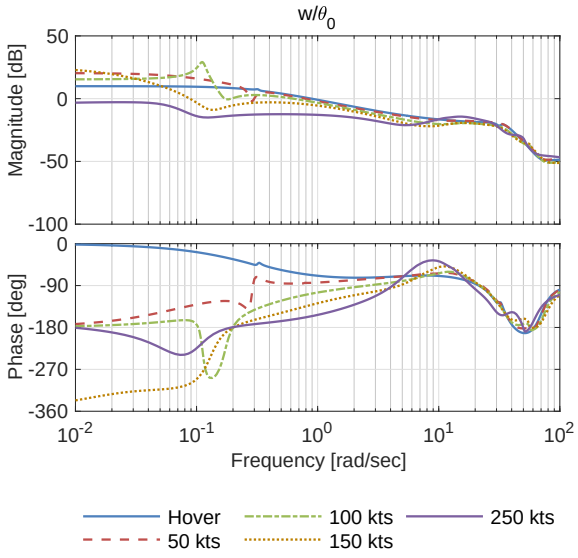

Figure 30: Vertical velocity frequency response (coaxial-pusher).

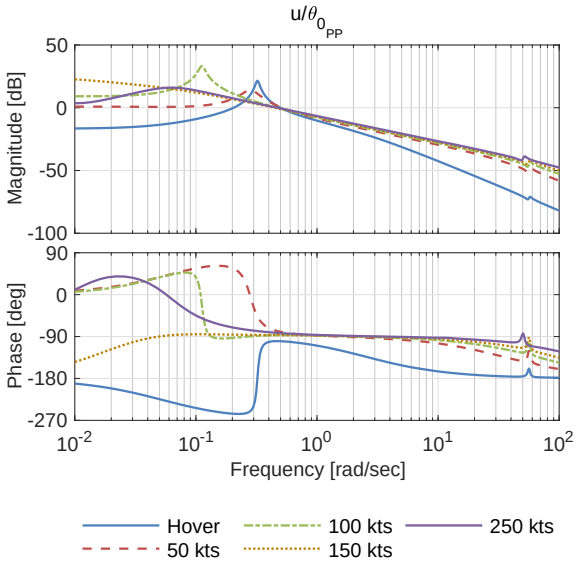

Figure 31: Longitudinal velocity frequency response (coaxial-pusher).

demand δ_{lon} frequency responses between hover and 250 kts. In hover, the pitch phugoid mode is at a frequency of $\omega_{\text{ph}} = 0.3$ rad/sec and is unstable. it is followed by a real pole at $\omega = -M_q = 2$ rad/sec. The regressive flap mode can be seen as the peak at $\omega = 12$ rad/sec (corresponding to the eigenvalue labeled "Regressive Flap + q" in Figure 10), followed by the progressive flap mode at $\omega = 50$ rad/sec.

As airspeed increases, the phugoid mode decreases in frequency and becomes stable. The short period mode is composed of two real poles, one stable and one unstable (corresponding to the eigenvalues labeled "Short Period" and "Pitch" in Figure 11) with increasing frequency as airspeed increases. As with the roll response, the regressive flap mode increases in frequency with increasing airspeed while the progressive flap mod decreases in frequency.

Figure 29 shows the yaw rate r to yaw moment demand δ_{ped} frequency responses between hover and 250 kts. In hover, below $\omega = 10$ rad/sec, the yaw rate response is first-order with a break frequency of $\omega = -N_r = 0.1$ rad/sec. One of the two collective lag modes (antisymmetric between the two rotors) can be seen at $\omega = 37$ rad/sec, due to differential collective $\Delta\theta_0$ being used for yaw control in hover. As airspeed increases, the Dutch roll mode can be seen in the yaw rate response as the peak between $\omega = 0.7 - 2$ rad/sec.

Figure 30 shows the z-axis body velocity w to symmetric collective θ_0 frequency responses between hover and 250 kts. In hover, below $\omega = 10$ rad/sec, the response is first-order with a break frequency of $\omega = -Z_w = 0.3$ rad/sec. The second collective lag mode (symmetric between the two rotors) can be seen at $\omega = 34$ rad/sec. As airspeed increases, the phugoid mode can be seen as the low-frequency distortion in the w frequency response, as well as the unstable short-period pole.

Figure 31 shows the x-axis body velocity u to pusher propeller collective $\theta_{0_{\text{PP}}}$ frequency responses between hover and 250 kts. In hover, the unstable longitudinal phugoid can be seen at $\omega_{\text{ph}} = 0.3$ rad/sec. In addition, the control power of the pusher propeller collective is lowest in hover, as seen by the low magnitude of the high-frequency asymptote as compared to the higher-airspeed responses. This also corresponds to the variation of the $X_{\theta_{0_{\text{PP}}}}$ control derivative seen in Figure 7. As airspeed increases, the control power of the pusher propeller increases in magnitude and the phugoid mode decreases in frequency.

4.3. Tiltrotor

Figures 32 through 36 show the primary on-axis frequency responses of the tiltrotor stitched model. Figure 32 shows the roll rate p to roll moment demand δ_{lat} frequency responses between hover and 250 kts. In hover with nacelles at $\delta_{\text{nac}} = 90$ deg, the roll rate response exhibits the unstable lateral phugoid at $\omega = 0.5$ rad/sec, with the roll mode real pole at a similar frequency $1/T_{\text{r}} = -L_p = 0.5$ rad/sec. The tiltrotor roll mode is at a lower frequency than the coaxial-pusher model ($1/T_{\text{r}} = 5$ rad/sec) due to the significantly larger roll-axis inertia I_{xx} of the tiltrotor with its engines and rotors at the wingtips. The collective rotor Mode 1 can be seen as the peak at $\omega = 45$ rad/sec. At $V = 50$ kts with nacelles at $\delta_{\text{nac}} = 90$ deg, the lateral phugoid is still unstable, and above $\omega = 1$ rad/sec, the response is very similar to that in hover.

As airspeed increases and the nacelles are brought down, the roll-rate response looks like a typical fixed-wing response, with the ω_ϕ zeros and Dutch roll mode poles around $\omega = 1 - 3$ rad/sec. In addition, since differential collective is phases out for roll control at higher airspeeds and differential longitudinal cyclic is phased in (Figure 25), the collective rotor Mode 1 is not present at the higher speed roll rate responses. Instead, the progressive rotor Mode 1 can be seen at $\omega = 75$ rad/sec.

Figure 33 shows the pitch rate q to pitch moment demand δ_{lon} frequency responses between hover and 250 kts. In hover, the pitch phugoid mode is at a frequency of $\omega_{\text{ph}} = 0.6$ rad/sec and is unstable. It is followed by a real pole at $\omega = -M_q = 0.7$ rad/sec. The coupled rotor modes can be seen between $\omega = 10 - 100$ rad/sec. As airspeed increases to $V = 50$

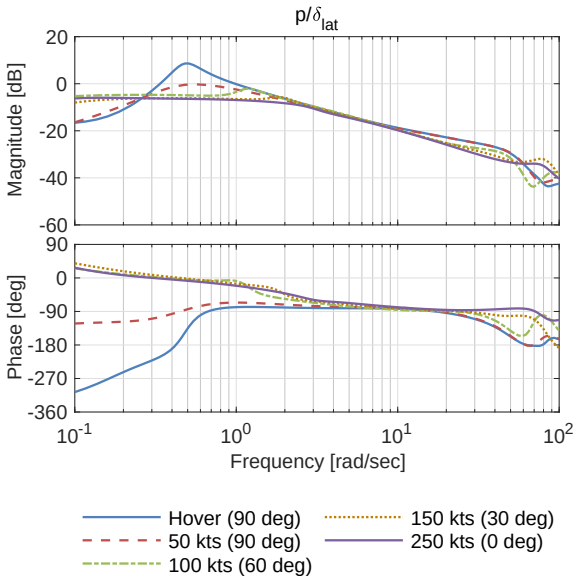

Figure 32: Roll rate frequency response (tiltrotor).

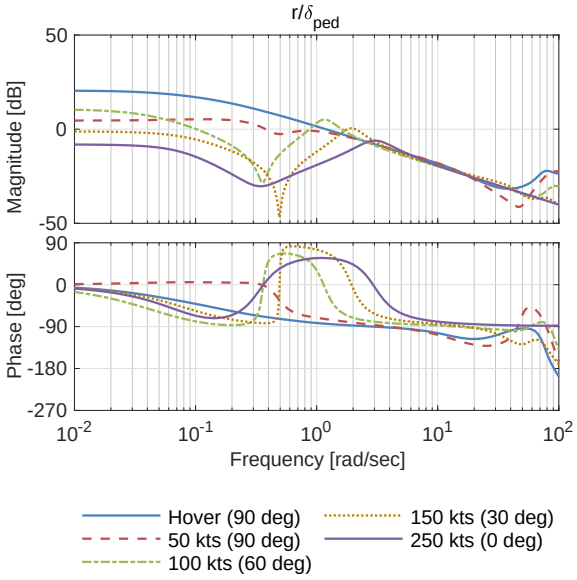

Figure 34: Yaw rate frequency response (tiltrotor).

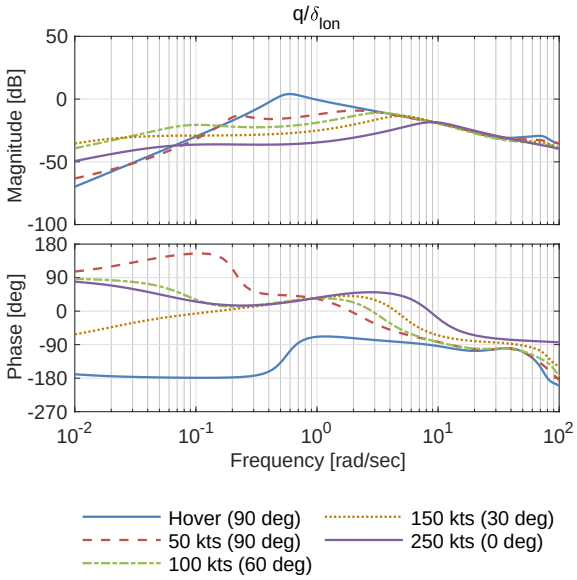

Figure 33: Pitch rate frequency response (tiltrotor).

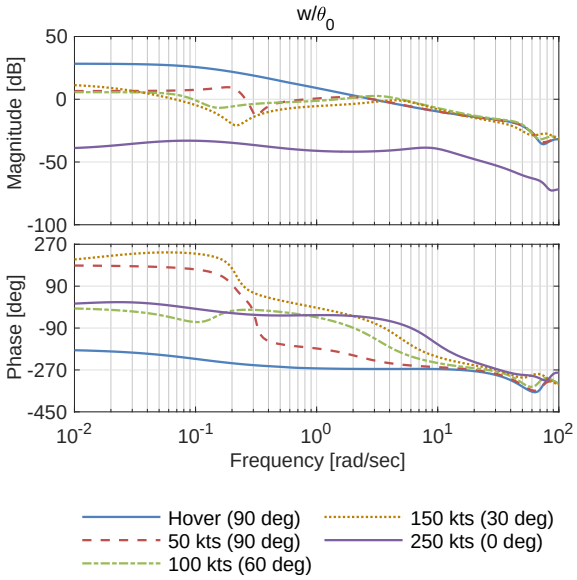

Figure 35: Vertical velocity frequency response (tiltrotor).

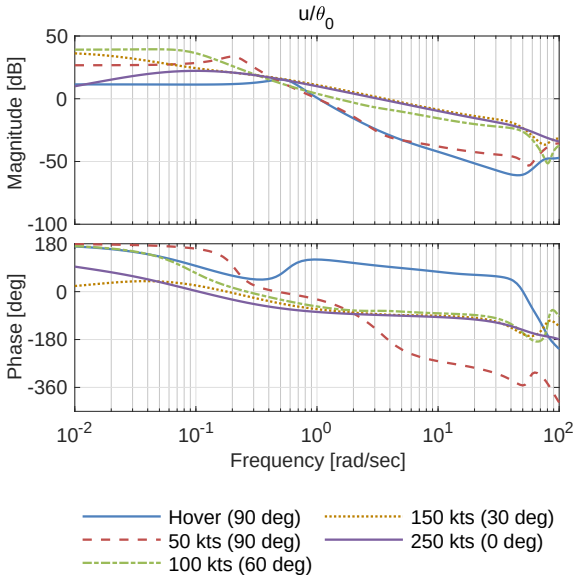

Figure 36: Longitudinal velocity frequency response (tiltrotor).

kts, the phugoid mode decreases in frequency and becomes stable. Above $V = 50$ kts, the complex phugoid mode splits into two real poles. For nacelle angle $\delta_{\text{nac}} = 30$ deg, there is a low-frequency unstable phugoid pole. Unlike the coaxial-pusher, the short period mode of the tiltrotor remains stable at all airspeeds.

Figure 34 shows the yaw rate r to yaw moment demand δ_{ped} frequency responses between hover and 250 kts. In hover, below $\omega = 30$ rad/sec, the yaw rate response is first-order with a break frequency of $\omega = -N_r = 0.12$ rad/sec. A coupled rotor mode can be seen at $\omega = 80$ rad/sec. As airspeed increases, the Dutch roll mode can be seen in the yaw rate response as the peak between $\omega = 1 - 4$ rad/sec.

Figure 35 shows the z-axis body velocity w to symmetric collective θ_0 frequency responses between hover and 250 kts. In hover, below $\omega = 10$ rad/sec, the response is first-order with a break frequency of $\omega = -Z_w = 0.15$ rad/sec. The coupled rotor modes can be seen between $\omega = 10 - 100$ rad/sec. As airspeed increases, the phugoid mode can be seen as the low-frequency distortion in the z-axis body velocity w frequency response. Furthermore, as expected, collective becomes less effective at generating z-axis body velocity w as nacelle angle decreases, with the $\delta_{\text{nac}} = 0$ deg response have a magnitude around 60 dB lower than the $\delta_{\text{nac}} = 90$ deg response.

Figure 36 shows the x-axis body velocity u to symmetric collective θ_0 frequency responses between hover and 250 kts. In hover, the unstable longitudinal phugoid can be seen at $\omega_{\text{ph}} = 0.6$ rad/sec. For nacelle angles $\delta_{\text{nac}} = 90$ deg, increasing collective results in a short-term decrease in x-axis body velocity u (operating on the "back side" of the power curve). Here, airspeed should be controlled with pitch attitude, like a typical helicopter. As the nacelle angle is decreased ($\delta_{\text{nac}} \leq 60$ deg), increasing collective results in a short-term increase in x-axis body velocity u (operating on the "front side" of the power curve).

5. DISCUSSION

5.1. Coaxial-Pusher

The coaxial-pusher configuration requires very large rotor cyclic control phasing to reduce off-axis flapping. To trim and linearize the model in HeliUM, a constant phase angle of $\Delta_{\text{SP}} = 70$ deg was used (similar to values used for XH-59A[13]). The optimal phase angle, however, is a function of airspeed. In the XH-59A, the phase angle Δ_{SP} was controlled in flight by the pilot through beeper switches[13]. For the coaxial-pusher model described here, the pseudo inverse control allocation gave the optimal phase angle at each airspeed.

The coaxial-pusher has significant inter-axis coupling at hover/low-speed, as seen by its off-axis rigid body stability and control derivatives, despite having a symmetric configuration. Control coupling is accounted for by the pseudo inverse control allocation, however dynamic coupling may need to be accounted for in a control system.

The overall trim trends with airspeed for the coaxial-pusher model (shown in Sec. 2.2.2) match well with the X2 flight data presented in Ref. 5. In addition, roll rate and pitch rate frequency responses of the X2 identified from flight data presented in Ref. 5 have similar characteristics to the coaxial-pusher frequency responses shown in Sec. 4.2. For example, the phase in the hover roll rate response of the coaxial-pusher model (Figure 27) starts at $\varphi = -180$ deg at low frequency and then flattens out at $\varphi = -45$ deg at a frequency above the phugoid mode ($\omega \approx 1$ rad/sec). This is consistent with the flight-identified X2 frequency response shown in Figure 9 of Ref. 5.

The primary hover/low-speed yaw control (differential collective $\Delta\theta_0$) and primary high-speed yaw control (rudder δ_{rud}) are both less effective in the mid-speed range ($V = 40 - 100$ kts). Therefore, two additional yaw controls are used to provide the necessary yaw authority. Differential longitudinal cyclic $\Delta\theta'_{1s}$ is used between $V = 40 - 100$ kts

and pusher propeller monocyclic $\theta_{1c_{PP}}$ is used between $V = 40 - 180$ kts.

The large peaks associated with the rotor modes in the roll rate response (Figure 27) between $\omega = 20-50$ rad/sec will impact the maximum achievable crossover frequency and gain margin of a control system in this axis. A lag or notch filter will likely be necessary to meet stability margin requirements[32].

5.2. Tiltrotor

The tiltrotor configuration requires less rotor cyclic control phasing ($\Delta_{SP} = 50$) than the coaxial-pusher ($\Delta_{SP} = 70$). This is expected for the less stiff rotors of the tiltrotor (with the first coupled flap-lag tiltrotor blade mode at a lower frequency than the first flap coaxial-pusher blade mode) since rotor tip clearance is not an issue.

Like the coaxial-pusher, the tiltrotor configuration is symmetric. In the case of the tiltrotor, this symmetry translates to decoupled lateral/directional and longitudinal/heave responses at all airspeeds, as similary seen for the XV-15 tiltrotor[7].

The tiltrotor configuration does have large adverse roll due to rudder deflections at high speed, as a consequence of its high V-tail. Adverse roll is seen in the XV-15 as well, with its high H-tail configuration, however less than the tiltrotor presented here. For the XV-15 at $V = 170$ kts[7]:

$$\left.\frac{L_{\delta_r}}{N_{\delta_r}}\right|_{XV-15} = -0.32 \tag{4}$$

while, for the tiltrotor model presented here, that value is more than double:

$$\left.\frac{L_{\delta_r}}{N_{\delta_r}}\right|_{\text{Tiltrotor}} = -0.68 \tag{5}$$

This adverse roll should be accounted for through additional control mixing, potential use of differential collective $\Delta\theta_0$ for yaw control in airplane mode, or feedback control.

The tiltrotor frequency responses shown in Sec. 4.3 have similar characteristics to the flight-identified XV-15 frequency responses shown in Ref. 7. For example, the tiltrotor pitch rate frequency response in cruise ($V = 250$ kts, $\delta_{nac} = 0$ deg) shown in Figure 33 has a well-damped phugoid mode, which is also seen in the XV-15 pitch rate frequency response in cruise shown in Figure 11.8 of Ref. 7.

6. CONCLUSIONS

This paper described flight dynamics models of generic lift offset coaxial and tiltrotor aircraft developed in HeliUM. The models were developed to be used for flight dynamics, control system design, and handling qualities analysis research. The following conclusions are drawn:

1. The models for both aircraft showed good agreement with flight data for similar aircraft configurations. The coaxial-pusher model was compared to X2 flight data, while the tiltrotor model was compared to XV-15 flight data. Although the aircraft modeled in this paper are larger than the flight vehicles they were compared to, excellent agreement in trim trends and frequency response characteristics were seen. This gives confidence in using the models presented here for future flight control and handling qualities research for these types of advanced rotorcraft configurations.

2. Control allocation using weighted pseudo inverse worked well to allocate demanded moments between the multiple rotor and aerosurface controls as flight condition varied. In the case of the coaxial-pusher, the weighted pseudo inverse solution provided the optimal phasing of the cyclic rotor controls for the very stiff rotor.

3. Primary on-axis frequency responses were shown at several different flight condition. Both aircraft have classical helicopter frequency responses in hover, with unstable low-frequency pitch and roll hovering cubics, and rotor modes at high frequency. At high speed, both aircraft exhibit classical fixed-wing responses. Namely, a lightly-damped Dutch roll mode is presented in the lateral/direction axes for both aircraft. In addition, both aircraft have well-damped phugoid modes at high speed. In the case of the coaxial-pusher, the short period mode was composed of two real poles, with one being unstable.

4. Finally, inherent inter-axis coupling is present in both designs despite their symmetric configurations. In the case of the coaxial-pusher, pitch-roll coupling is most pronounced at hover/low-speed and is significantly reduced at high speed, like typical helicopter configurations. In the case of the tiltrotor, large adverse roll-yaw coupling to rudder inputs is present at high speed due to the tail configuration. For both configurations, coupling should be addressed in the control system design.

REFERENCES

[1] Anon., "Joint Multi-Role Technology Demonstrator Phase 1 Broad Area Anouncement," January 2013.

[2] Anon., "Model Performance Specification for the Joint Multi-Role, Rev 6," January 2013.

[3] Juhasz, O., Celi, R., Ivler, C. M., Tischler, M. B., and Berger, T., "Flight Dynamic Simulation Modeling of Large Flexible Tiltrotor Aircraft," American Helicopter Society 68th Annual Forum Proceedings, May 2012, Fort Worth, TX.

[4] Celi, R., "HeliUM 2 Flight Dynamic Simulation Model: Developments, Technical Concepts, and Applications," American Helicopter Society 71st Annual Forum, May 2015, Virginia Beach, VA.

[5] Fegely, C., Xin, H., Juhasz, O., and Tischler, M. B., "Flight Dynamics and Control Modeling with System Identification Validation of the Sikorsky X2 Technology Demonstrator," American Helicopter Society 72nd Annual Forum Proceedings, May 2016, West Palm Beach, FL.

[6] Tobias, E. L. and Tischler, M. B., "A Model Stitching Architecture for Continuous Full Flight-Envelope Simulation of Fixed-Wing Aircraft and Rotorcraft from Discrete-Point Linear Models," U.S. Army AMRDEC Special Report RDMR-AF-16-01, April 2016.

[7] Tischler, M. B. and Remple, R. K., *Aircraft and Rotorcraft System Identification: Engineering Methods with Flight Test Examples*, AIAA, 2nd ed., 2012, Reston, VA.

[8] Marcos, A. and Balas, G. J., "Development of Linear-Parameter-Varying Models for Aircraft," *AIAA Journal of Guidance, Control, and Dynamics*, Vol. 27, No. 2, March-April 2004.

[9] Peters, D. A. and He, C. J., "Correlation of Measured Induced Velocities with a Finite-State Wake Model," *Journal of the American Helicopter Society*, Vol. 36, No. 3, July 1991, pp. 59–70.

[10] Johnson, W., "Technology Drivers in the Development of CAMRAD II," American Helicopter Society Aeromechanics Specialists Conference Proceedings, January 1994, San Francisco, CA.

[11] Johnson, W., Moodie, A. M., and Yeo, H., "Design and Performance of Lift-Offset Rotorcraft for Short-Haul Missions," American Helicopter Society Future Vertical Lift Aircraft Design Conference Proceedings, January 2012, San Francisco, CA.

[12] Hersey, S., Celi, R., Juhasz, O., and Tischler, M. B., "Accurate State-Space Inflow Modeling for Flight Dynamics and Control of a Coaxial-Pusher Rotorcraft," AHS International 74th Annual Forum Proceedings, May 2018, Phoenix, AZ.

[13] Ruddell, A. J., "Advancing Blade Concept (ABC) Technology Demonstrator," USAAVRADCOM TR-81-D-5, April 1981.

[14] Juhasz, O., Syal, M., Celi, R., Khromov, V., Rand, O., Ruzicka, G. C., and Strawn, R. C., "Comparison of Three Coaxial Aerodynamic Prediction Methods Including Validation with Model Test Data," *Journal of the American Helicopter Society*, Vol. 59, No. 3, July 2014.

[15] Ferguson, S. W., "A Mathematical Model for Real Time Flight Simulation of a Generic Tilt-Rotor Aircraft," NASA CR 166536, September 1988.

[16] Bailey Jr., F. J., "A Simplified Theoretical Method of Determining the Characteristics of a Lifting Rotor in Forward Flight," NACA-TR 716, January 1941.

[17] Padfield, G. D., *Helicopter Flight Dynamics: The Theory and Application of Flying Qualities and Simulation Modeling*, AIAA, 2nd ed., 2007, Reston, VA.

[18] Blackwell, R. and Millott, T., "Dynamics Design Characteristics of the Sikorsky X2 Technology Demonstrator Aircraft," American Helicopter Society 64th Annual Forum Proceedings, May 2008, Montreal, Canada.

[19] Leishman, J. G., *Principles of Helicopter Aerodynamics*, Cambridge University Press, 2nd ed., 2006, New York, NY.

[20] Harendra, P. B., Joglekar, M. J., Gaffey, T. M., and Marr, R. L., "Final Report V/STOL Tilt Rotor Study - Volume V: A Mathematical Model for Real Time Flight Simulation of the Bell Model 301 Tilt Rotor Research Aircraft," NASA CR 114614, April 1973.

[21] Maisel, M., "NASA/Army XV-15 Tilt Rotor Research Aircraft Familiarization Document," NASA TM X-62,407, January 1976.

[22] Acree, C. W. and Tischler, M. B., "Determining XV-15 Aeroelastic Modes from Flight Data with Frequency-Domain Methods," NASA/TP 3330, May 1993.

[23] Brunken, J. E., Popelka, D. A., and Bryson, R. J., "A Review of the V-22 Dynamics Validation Program," American Helicopter Society 45th Annual Forum Proceedings, May 1989, Boston, MA.

[24] Acree, C. W. and Johnson, W., "Aeroelastic Stability of the LCTR2 Civil Tiltrotor," American Helicopter Society Technical Specialist's Meeting Proceedings, October 2008, Dallas, TX.

[25] Acree, C. W., Yeo, H., and D, S. J., "Performance Optimization of the NASA Large Civil Tiltrotor," NASA TM 215359, June 2008.

[26] Ivler, C. M. and Juhasz, O., "Evaluation of Control Allocation Techniques for Medium Lift Tilt-

Rotor," American Helicopter Society 71st Annual Forum Proceedings, May 2015, Virginia Beach, VA.
[27] Subrahmanyam, K. B. and Kaza, K. R. V., "Nonlinear Flap-Lag-Extensional Vibrations of Rotating, pretwisted, Preconed Beams Including Coriolos Effects," NASA TM 87102, September 1985.
[28] Shupe, N. K., "A Study of the Dynamic Motions of Hingeless Rotored Helicopters," US Army Electronics Command TR ECOM- 3323, August 1970, Fort Monmouth, NJ.
[29] Enns, D., "Control Allocation Approaches," AIAA Guidance, Navigation and Control Conference, August 1998, Boston, MA.
[30] Anon., "Flying Qualities of Piloted Aircraft," MIL-STD-1797B, Department of Defense Interface Standard, February 2006.
[31] McRuer, D. T., Ashkenas, I. L., and Graham, D., *Aircraft Dynamics and Automatic Control*, Princeton University Press, 1973, Princeton, NJ.
[32] Anon., "Aerospace - Flight Control Systems - Design, Installation and Test of Piloted Military Aircraft, General Specification For," SAE-AS94900, July 2007.